PAPER

Structure, ligands and substrate coordination of the oxygen-evolving complex of photosystem II in the S₂ state: a combined EPR and DFT study†

Thomas Lohmiller,[a] Vera Krewald,[a] Montserrat Pérez Navarro,[a] Marius Retegan,[a] Leonid Rapatskiy,[a] Marc M. Nowaczyk,[b] Alain Boussac,[c] Frank Neese,[a] Wolfgang Lubitz,[a] Dimitrios A. Pantazis*[a] and Nicholas Cox*[a]

The S₂ state of the oxygen-evolving complex of photosystem II, which consists of a Mn_4O_5Ca cofactor, is EPR-active, typically displaying a multiline signal, which arises from a ground spin state of total spin $S_T = 1/2$. The precise appearance of the signal varies amongst different photosynthetic species, preparation and solvent conditions/compositions. Over the past five years, using the model species *Thermosynechococcus elongatus*, we have examined modifications that induce changes in the multiline signal, *i.e.* Ca^{2+}/Sr^{2+}-substitution and the binding of ammonia, to ascertain how structural perturbations of the cluster are reflected in its magnetic/electronic properties. This refined analysis, which now includes high-field (W-band) data, demonstrates that the electronic structure of the S₂ state is essentially invariant to these modifications. This assessment is based on spectroscopies that examine the metal centres themselves (EPR, ⁵⁵Mn-ENDOR) and their first coordination sphere ligands (¹⁴N/¹⁵N- and ¹⁷O-ESEEM, -HYSCORE and -EDNMR). In addition, extended quantum mechanical models from broken-symmetry DFT now reproduce all EPR, ⁵⁵Mn and ¹⁴N experimental magnetic observables, with the inclusion of second coordination sphere ligands being crucial for accurately describing the interaction of NH_3 with the Mn tetramer. These results support a mechanism of multiline heterogeneity reported for species differences and the effect of methanol [*Biochim. Biophys. Acta, Bioenerg.*, 2011, **1807**, 829], involving small changes in the magnetic connectivity of the solvent accessible outer Mn_{A4} to the cuboidal unit Mn_3O_3Ca, resulting in predictable changes of the measured effective ⁵⁵Mn hyperfine tensors. Sr^{2+} and NH_3 replacement both affect the observed ¹⁷O-EDNMR signal envelope supporting the assignment of O5 as the exchangeable μ-oxo bridge and it acting as the first site of substrate inclusion.

1 Introduction

In oxygenic photosynthesis, light-driven water oxidation is catalysed by the oxygen-evolving complex (OEC) of the transmembrane protein complex photosystem II (PSII). The OEC

[a] *Max-Planck-Institut für Chemische Energiekonversion, Stiftstrasse 34-36, D-45470 Mülheim an der Ruhr, Germany. E-mail: dimitrios.pantazis@cec.mpg.de, nicholas.cox@cec.mpg.de; Fax: +49 208 306 3955; Tel: +49 208 306 3552*

[b] *Ruhr-University Bochum, Universitätsstrasse 150, D-44780 Bochum, Germany*

[c] *iBiTec-S, SB2SM, UMR 8221, CEA Saclay, 91191 Gif-sur-Yvette, France*

† Electronic supplementary information (ESI) available: PSII sample preparation; data processing: baseline correction and light-minus-dark subtraction; spectral simulations; theoretical background; DFT calculations: NH_3 binding modes and spatial coordinates of the S₂ state models; Q-band ⁵⁵Mn-ENDOR: comparison of instrumental settings; electronic structures: exchange couplings and spin states of the BS-DFT models; the Mn_{D1}–His332-imino-N interaction: Q-band three-pulse ESEEM, Q-band HYSCORE, W-band EDNMR and simulations; X-band ¹⁴N- and ¹⁵N-three pulse ESEEM experiments on the NH_3-modified S₂ state; exchangeable ¹⁷O species: W-band EDNMR and X-band EPR. See DOI: 10.1039/c3cp55017f

consists of a μ-oxo-bridged tetramanganese-calcium cofactor (Mn_4O_5Ca), embedded in its protein matrix. This matrix includes the redox-active tyrosine residue Y_Z (D1-Tyr161), which couples electron transfer between the Mn_4O_5Ca cluster and P680•⁺, the photooxidant of the PSII reaction centre. The four-electron water oxidation reaction requires four consecutive light-induced charge separation events, driving the catalytic cycle of the OEC.[1,2] This cycle involves five redox intermediates, the S_n states, where $n = 0$–4 indicates the number of stored oxidizing equivalents. All S-state transitions represent oxidations of the Mn_4O_5Ca cluster by Y_Z• with the exception of the regeneration of S₀ from S₄, which proceeds spontaneously under the release of molecular triplet oxygen and the rebinding of at least one substrate water molecule. The rate-limiting step, oxidation of S₃ by Y_Z•, has prevented the transient, fast-decaying S₄ state from being characterized yet. For a general introduction into water oxidation by the OEC, see ref. 3–8.

The structure of the Mn_4O_5Ca inorganic core[9] resembles a 'distorted chair' where the base is formed by a μ-oxo-bridged

This journal is © the Owner Societies 2014

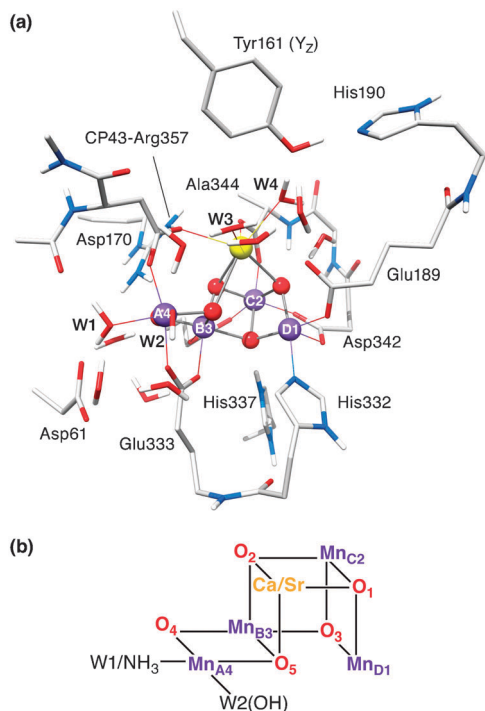*Phys. Chem. Chem. Phys.,* 2014, **16**, 11877–11892 | **11877**

Fig. 1 (a) DFT cluster model of the native OEC and its immediate surrounding in the S_2 (S_T = 1/2) state. Mn ions are depicted in purple, O in red, Ca in yellow, C in light grey, N in blue and H in white; most H atoms are omitted for clarity. (b) $Mn_4O_5Ca/Sr–H_2O/NH_3$ cores showing the atom and ligand labels used in this work.

cuboidal Mn_3O_4Ca unit (Fig. 1), while the fourth, 'outer' Mn, Mn_{A4} is attached to this core structure *via* two μ-oxo bridges, O4 and O5. Spectroscopic evidence suggests that all five oxygen bridges are deprotonated in the S_2 state.[10–15] In addition to the μ-oxo-bridged network, the Mn_4O_5Ca scaffold is held together by six carboxylate ligands, four of which (D1-Asp342, D1-Asp170, D1-Glu333 and CP47-Glu354) form μ-carboxylato bridges between Mn sites. The cluster has only one immediate nitrogen ligand, the imidazole imino-N of D1-His332.

An understanding of the mechanism of water oxidation catalysis is intimately linked to an understanding of the electronic states of the paramagnetic tetranuclear Mn complex. Electron paramagnetic resonance (EPR) spectroscopy represents a powerful methodology in this endeavour.[16–19] The S_2 state, being readily generated from the dark-stable S_1 state, is the most extensively characterized S state by EPR. It is intrinsically heterogeneous,[20–22] existing in two ground state configurations. The lowest energy form exhibits a ground state of total spin S_T = 1/2. This spin configuration gives rise to the well-known S_2 state EPR multiline signal centred at $g \approx 2.0$, with a hyperfine pattern of at least 24 peaks, with a line spacing around 87 G.[23] Depending on the conditions used, the S_2 state can also exhibit other broad EPR signals, centred at $g \geq 4.1$, which have been assigned to (an) $S_T \geq 5/2$ spin state(s).[20,24–28] The $g \geq 4.1$ signal can also be induced by near-infrared illumination of the S_2 multiline state at temperatures ≤ 160 K.[24,25,29] Pulse electron nuclear double resonance (ENDOR) experiments,[30] especially at Q-band

frequencies,[31–34] have enabled a more detailed examination of the electronic structure by uniquely determining four ^{55}Mn hyperfine interactions that give rise to the multiline pattern of the corresponding S_T = 1/2 EPR signal. This ENDOR analysis has strongly suggested that the OEC contains one Mn^{III} ion and three Mn^{IV} ions when poised in the S_2 state.[30–34]

OEC models developed from broken-symmetry (BS) density functional theory (DFT) have been crucial for the interpretation of EPR and related magnetic resonance results.[12,14,18,33,35–44] These calculations now allow different S-state models to be assessed based on the spin multiplicities and relative energies of their lowest magnetic levels, and, by means of the spin projection formalism (see ref. 18 and 36), the metal and ligand hyperfine couplings. This strategy enables the assignment of individual Mn oxidation states and coordination geometries and represents a method to develop unified models of the OEC that combine constraints from X-ray diffraction, EXAFS and magnetic resonance.

Site perturbation of the OEC provides a means to further characterize the global geometric and electronic structure of the Mn tetramer and obtain information about localized changes associated with the introduced modification. The two best described OEC perturbations in the literature are (i) the replacement of the Ca^{2+} with a Sr^{2+} ion[33,45–47] and (ii) the binding of NH_3 to the cluster.[48–55] Both of these perturbations *do not* inhibit functional turnover of the catalyst, but do modify the kinetics of O–O bond formation, substrate water uptake and its subsequent deprotonation. A brief description of these two modified OEC forms is given below:

(i) Sr^{2+} can be introduced into the OEC through chemical removal of the Ca^{2+} ion[45,46,56] or alternatively by biosynthetic incorporation in cyanobacterial cultures grown in the presence of $SrCl_2$ instead of $CaCl_2$.[47] Without Ca^{2+} (or Sr^{2+}) the OEC is inhibited,[56–63] not progressing further than a modified form of the S_2 state, *i.e.* the $S_2'Y_Z^\bullet$ state.[60–62] Sr^{2+} is unique as it is the only ion which can replace the Ca^{2+} ion while retaining catalytic activity, albeit at a lower enzymatic rate.[45,47,56] Presumably this is because Sr^{2+} has a similar size and Lewis acidity as Ca^{2+}.[64] While slowing the turnover rate of the catalyst, Sr^{2+} substitution at the same time enhances the exchange rate with bulk water of at least one of the bound substrates,[65,66] as observed by time-resolved membrane inlet mass spectrometry (MIMS).[67,68] This behaviour suggests the Ca^{2+} ion may play an important role in substrate water binding and possibly proton release (for reviews, see ref. 3 and 69).

(ii) Ammonia binding to the Mn cluster (in the presence of high Cl^- concentrations)[48,50,51,54] only occurs upon formation of the S_2 state. It is subsequently released at some point during the S-state cycle ($S_3 \rightarrow S_0 \rightarrow S_1$), such that it is not bound upon return to S_1.[51] As with Sr^{2+} replacement, NH_3 binding does not inhibit catalytic function. In the higher plant electron spin echo envelope modulation (ESEEM) study of Britt *et al.*,[70] NH_3 was shown to bind as a direct ligand of the Mn tetramer. The precise binding site and coordination mode of the NH_3 molecule was the subject of a recent study on cyanobacterial PSII from our laboratory.[44] By employing electron electron double resonance (ELDOR)-detected NMR (EDNMR), it was concluded that NH_3

11878 | *Phys. Chem. Chem. Phys.*, 2014, **16**, 11877–11892

This journal is © the Owner Societies 2014

replaces the water ligand of Mn_{A4} *trans* to the O5 bridge (W1, Fig. 1b). As the binding of NH_3 was also shown not to affect substrate exchange rates, these results suggest W1 does not represent a substrate water. One or more additional NH_3 binding sites, which are inhibitory, are known but are less well characterized.[49,50,71]

Here, we present an extension of our earlier multifrequency EPR studies[33,34,44] of different 'archetypal' multiline forms, namely the native (Mn_4O_5Ca), Sr^{2+} substituted (Mn_4O_5Sr) and NH_3-treated ($Mn_4O_5Ca-NH_3$) S_2 states, providing a comprehensive analysis of all present X-, Q- and W-band data of ^{55}Mn, $^{14}N/^{15}N$ and ^{17}O signals and for the first time including additional data on the doubly modified ($Mn_4O_5Sr-NH_3$) S_2 state. Improved ^{55}Mn ENDOR experimental conditions provide more reliable spectral line shapes than before, confirming our previous general S_2 state model. Extended BS-DFT models are shown to reproduce all EPR, ^{55}Mn and ^{14}N magnetic spectroscopic observables for the native and the modified systems, a feature not achieved previously. The experimental results and calculations for $^{14}N/^{15}N$ ligands of the various S_2 state forms serve to prove that the basic electronic structure is not perturbed by these modifications, a result crucial for the interpretation of concomitant perturbations of the ^{17}O EDNMR signal envelope. This combined experimental and theoretical approach supports our qualitative model for multiline heterogeneity, demonstrating that the magnetic connectivity between the two subunits and also within the trimeric moiety governs the structure of the multiline signal.[34] This basic structural template also explains the apparent orientations of the ^{55}Mn hyperfine tensors, as inferred from spectral simulations and single crystal measurements,[32] and potentially provides a framework to further examine substrate binding. The different OEC forms represent a starting point to examine the energetics of higher S-state transitions, as they differ with regard to substrate binding and the kinetics of O–O bond formation and O_2 release.

2 Materials and methods

2.1 PSII sample preparation

Ca^{2+}- and Sr^{2+}-containing PSII core complex preparations from *T. elongatus*[72] were isolated as reported before[47,73,74] with the same modifications for the X-band samples as described in ref. 44. Universal ^{15}N-labelling of the PSII proteins was achieved by growing the cyanobacteria in a modified BG11 or DTN medium that contained $^{15}NH_4Cl$ and $^{15}NO_3^-$ salts as the sole nitrogen source.[75] PSII preparations were stored at $-80\ ^\circ C$ until use. Dark-adapted samples were placed in X-, Q- or W-band quartz tubes with inner diameters of 3.0, 1.6 and 0.6 mm, respectively, and kept at 77 K (liquid N_2) until use. A sample concentration of 3.0–4.0 mg chlorophyll per ml was used throughout this study. All work was conducted in the dark or under dim green light. NH_3 modification was conducted as described in ref. 44, see also Section S1 of the ESI.† Isotopically enriched $H_2^{17}O$ buffer exchange was achieved as described in ref. 14.

2.2 X-, Q-, and W-band EPR and ENDOR measurements

X-band (≈ 9 GHz) continuous-wave (CW) EPR spectra were recorded at liquid He temperatures on a Bruker ELEXSYS E500 spectrometer, equipped with an ESR 900 liquid helium flow cryostat and an ITC503 helium flow temperature controller (Oxford Instruments Ltd). X-band pulse EPR measurements were carried out at 4.3 K using a Bruker ELEXSYS E580 spectrometer, equipped with a CF935 cryostat and an ITC503 temperature controller. Q-band (≈ 34 GHz) pulse EPR measurements were performed around 5 K using an ELEXSYS E580 spectrometer, equipped with a homebuilt TE_{011} microwave cavity,[76] a CF935 liquid helium cryostat, an ITC-503 temperature controller and a radiofrequency (RF) amplifier ENI 5100L. W-band (≈ 94 GHz) EPR experiments were performed at 4.8 K using a Bruker ELEXSYS E680 EPR spectrometer. All W-band experiments were carried out using a homebuilt ENDOR microwave cavity, which contained a solenoid of Teflon coated silver wire integrated into a commercial ENDOR probe head (Bruker). In order to ensure broadband microwave excitation and minimize distortions, the loaded quality factor Q_L was lowered to 700 to obtain a microwave frequency bandwidth of 130 MHz.

Electron spin echo-detected (ESE) field-swept EPR spectra were measured using the pulse sequence $t_p-\tau-2t_p-\tau-echo$,[77] three-pulse ESEEM spectra by use of $t_p-\tau-t_p-T-t_p-\tau-echo$[78] and hyperfine sublevel correlation (HYSCORE) spectra by employing $t_p-\tau-t_p-T_1-2t_p-T_2-t_p-\tau-echo$.[79] The lengths of the $\pi/2$ microwave pulses were generally set to $t_p = 16$ ns (X-band), 12 ns (Q-band) and 24 ns (W-band), respectively. For ESE-detected EPR experiments, inter-pulse distances were $\tau = 260$ ns (Q-band) and 300 ns (W-band). For the three-pulse ESEEM measurements, multiple τ values in the ranges $\tau = 136$–248 ns (X-band) and 200–356 ns (Q-band) and an optimum $\tau = 260$ ns for the HYSCORE experiments were chosen to account for blind-spotting artefacts. Q-band ^{55}Mn-ENDOR spectra were acquired employing the Davies-type pulse sequence $t_{inv}-t_{RF}-T-t_p-\tau-2t_p-\tau-echo$[80] using a length $t_{inv} = 24$ ns for the π inversion microwave pulse and a radio frequency π pulse length $t_{RF} = 3.5\ \mu s$. The length of the $\pi/2$ microwave pulse in the detection sequence was generally set to $t_p = 12$ ns and the inter-pulse delays to $T = 2\ \mu s$ and $\tau = 268$ ns. A shot repetition time of 1 ms was used for all measurements. EDNMR measurements were collected using the pulse sequence $t_{HTA}-T-t_p-\tau-2t_p-\tau-echo$.[81] The high turning angle (HTA) microwave pulse was applied at microwave frequencies ν_{mw}. The Hahn echo detection pulse sequence $t_p-\tau-2t_p-\tau-echo$, at a microwave frequency $\nu_{mw}^{(0)}$ matched to the cavity resonance, was set at a sufficient time T after the HTA pulse to ensure near-complete decay of the electron spin coherencies. The $\pi/2$ pulse length used for detection was $t_p = 200$ ns (^{14}N, ^{17}O) or 80 ns (^{15}N) and an inter-pulse separation of $\tau = 500$ ns was used. The echo was integrated ≈ 600 ns around its maximum. The spectra were acquired *via* continuously sweeping the HTA frequency ν_{mw} at a fixed magnetic field in steps of 78.1 kHz (^{14}N), 128.9 kHz (^{15}N) or 162.1 kHz (^{17}O). A HTA microwave pulse of length $t_{HTA} = 14\ \mu s$ (^{14}N, ^{17}O) and 8 μs (^{15}N) and an amplitude $\omega_1 = 12$–16×10^6 rad s^{-1} was used.

This journal is © the Owner Societies 2014

Phys. Chem. Chem. Phys., 2014, **16**, 11877–11892 | 11879

2.3 Spectral simulations

Spectra were fit assuming an effective spin $S_T = 1/2$ ground state (Section S4.2, ESI†). The basis set that describes the ^{55}Mn tetramer-single electron spin manifold (eqn (1)) and the ^{14}N, ^{15}N and ^{17}O single nucleus-single electron spin manifolds (eqn (2)) can be built from the product of the eigenstates of the interacting spins:

$$|\tfrac{1}{2}MI_1m_1I_2m_2I_3m_3I_4m_4\rangle \qquad (1)$$

$$|\tfrac{1}{2}MIm\rangle \qquad (2)$$

Here, M refers to the electronic magnetic sublevel, $\pm\tfrac{1}{2}$; I takes the values $5/2$ for ^{55}Mn, 1 for ^{14}N, $\tfrac{1}{2}$ for ^{15}N and $5/2$ for ^{17}O; m_i takes the values $-I_i, 1 - I_i, \ldots, I_i - 1, I_i$. The spin manifolds can be described by the following spin Hamiltonian:

$$\hat{H} = \beta_e \vec{B}_0 \cdot \hat{G} \cdot \vec{S} + \sum_i \left(-g_{n,i}\beta_n \vec{B}_0 \cdot \vec{I}_i + \vec{S} \cdot \hat{A}_i \cdot \vec{I}_i + \vec{I}_i \cdot \hat{Q}_i \cdot \vec{I}_i \right)$$

(3)

It contains (i) the Zeeman term for the total electronic spin, (ii) the hyperfine and (iii), except for the EPR spectra, nuclear Zeeman terms for either the metal ^{55}Mn nuclei, or the ligand ^{14}N, ^{15}N or ^{17}O nuclei and (iv), for the ^{14}N nuclei ($I = 1$), the nuclear quadrupole interaction (NQI) term; the NQI splitting is not resolved in the ^{55}Mn and ^{17}O spectra. Spectral simulations were performed numerically using MATLAB® (R2010a, The MathWorks, Natick, MA, USA), a vector-based linear algebra package, and the EasySpin toolbox.[82] For further information on data processing, details of the simulations and theory, see Sections S2, S3 and S4 (ESI†), respectively.

2.4 DFT calculations

All calculations were performed with ORCA.[83] The DFT models of the OEC systems consist of 238 or 239 atoms (with H_2O or NH_3 at the W1 position, respectively) and were constructed as described in Pantazis *et al.*[40] Alternative ammonia binding modes, including terminal or bridging amido and imido substitution, can be rejected on energetic grounds alone (see Fig. S2, ESI†). Geometry optimizations of the cluster models used the BP86 density functional[84,85] with the zeroth-order regular approximation (ZORA)[86–88] and specially adapted segmented relativistically recontructed basis sets[89] (ZORA-TZVP for Mn, O and N; ZORA-SVP for C and H). The conductor-like screening model (COSMO)[90] was used with a dielectric constant $\varepsilon = 8.0$. D3 dispersion corrections[91] were applied in all calculations. Exchange coupling constants, assuming an isotropic Heisenberg Hamiltonian of the form

$$\hat{H} = -2J_{ij} \sum_{i<j} \hat{S}_i \cdot \hat{S}_j, \qquad (4)$$

and all EPR properties were computed with the TPSSh hybrid meta-GGA functional[92,93] from BS-DFT calculations.[35,94–98] The resolution of identity (RI)[99] approximation was used in the calculation of Coulomb integrals and the chain-of-spheres approximation (COSX)[100] was used for Hartree–Fock exchange, employing completely decontracted def2-TZVP/J auxiliary basis sets.[101] Tight SCF

convergence criteria and increased integration grids (Grid6 and GridX6) were applied throughout.

For the calculation of the hyperfine tensors, triple-zeta ZORA-recontracted basis sets were used on all atoms, while locally dense radial grids were used for Mn, N and O atoms (integration accuracy of 11 for Mn and 9 for N and O as per ORCA nomenclature). Picture change effects were applied for the calculation of EPR parameters and the complete mean-field approach was used for the spin–orbit coupling operator. The results were transformed into on-site or spin-projected values as detailed previously.[36] To compare computed ^{55}Mn hyperfine coupling constants using the methods described above with experimental results, a scaling factor of 1.78 was calculated from a set of twelve $Mn^{III}Mn^{IV}$ mixed-valence dimers.[102]

3 Results and discussion

3.1 DFT models of different OEC forms in the S_2 state

Geometric parameters of optimized DFT cluster models of the S_2 state of the OEC in the $S_T = 1/2$ configuration[40] are shown in Fig. 2 (for coordinates, see Section S5, ESI†). Four variants were considered in this study: (i) the native cofactor system (Mn_4O_5Ca, also see Fig. 1), (ii) the Sr^{2+}-substituted system obtained by replacing Ca^{2+} with Sr^{2+} (Mn_4O_5Sr), (iii) the NH_3-modified system obtained by replacing the H_2O in the W1 position with NH_3 ($Mn_4O_5Ca–NH_3$), and (iv) the combined Sr^{2+}-substituted and NH_3-modified system ($Mn_4O_5Sr–NH_3$). In all models, W2 was considered to be an OH^- ligand, as determined previously.[12] Mulliken spin population analysis of all four variants confirms that the only Mn^{III} ion of the tetramanganese complex is Mn_{D1}. The three Mn^{IV} ions (Mn_{A4}, Mn_{B3} and Mn_{C2}) represent coordinatively saturated, 6-coordinate octahedral sites, whereas the $Mn_{D1}{}^{III}$ is 5-coordinate square-pyramidal, with a Jahn–Teller elongation along the axis of the Mn_{D1}-Asp342 carboxylate ligand, opposite to its open coordination site.

In accordance with previous DFT and QM/MM structures,[12,37,38,40–42,103–106] the optimized Mn–Mn and Mn–Ca distances of the Mn_4O_5Ca model are consistent with those determined from EXAFS spectroscopy.[107–110] Only minor changes are observed between the Mn_4O_5Ca and the Mn_4O_5Sr models (Fig. 2). As a result of the larger radius of Sr^{2+}, the O–Sr bond lengths increase by 0.04 Å, while the Mn–Sr distances also increase by 0.04 Å except for Mn_{D1}–Sr, which is 0.03 Å shorter than the Mn_{D1}–Ca distance. On average, this is in line with observations from EXAFS spectroscopy[108] and with the recent 2.1 Å resolution crystallographic model of Sr^{2+}-substituted PSII.[111] The Mn–Mn distances are almost entirely unaffected, with the exception of Mn_{D1}–Mn_{C2}, which is shortened by 0.02 Å in the Mn_4O_5Sr model.

Upon NH_3 substitution of W1 ($Mn_4O_5Ca–NH_3$), only the Mn_{D1}–Mn_{B3} distance and the Ca^{2+} distance from the terminal Mn ions change notably, albeit by less than 0.05 Å (Fig. 2). Only one structural element is more significantly perturbed, *i.e.* the position of O5, the μ-oxo bridge *trans* to the binding position of NH_3. The Mn_{A4}–O5 distance increases by 0.05 Å with concomitant

11880 | *Phys. Chem. Chem. Phys.*, 2014, **16**, 11877–11892

This journal is © the Owner Societies 2014

Mn$_4$O$_5$Ca

Mn$_4$O$_5$Sr

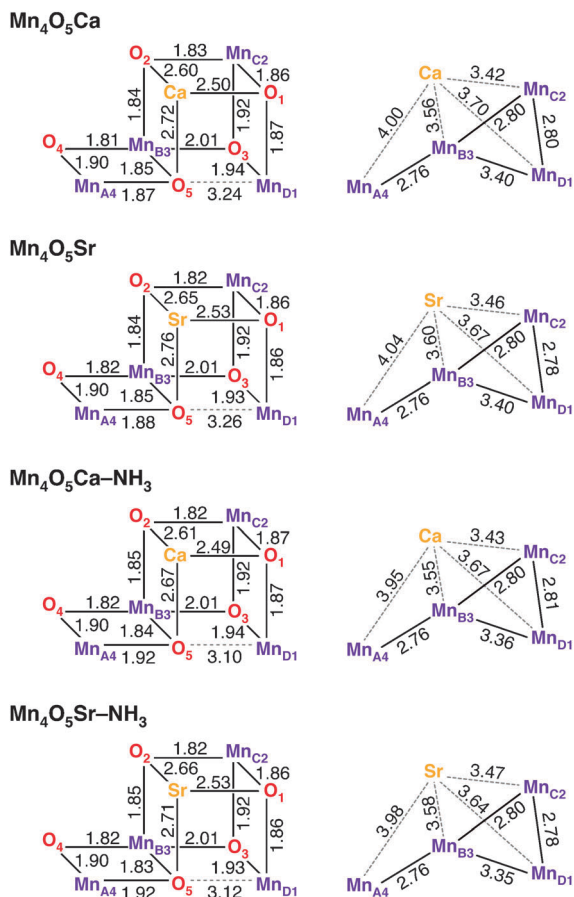**Mn$_4$O$_5$Ca–NH$_3$**

Mn$_4$O$_5$Sr–NH$_3$

Fig. 2 Bond lengths and metal–metal distances in Å of the four geometry-optimized DFT models.

decrease of the Mn$_{D1}$–O5 distance by 0.14 Å. Other ligands of Mn$_{A4}$, such as the second water-derived ligand, W2, remain unaffected. A similar modification to the connectivity of the Mn$_4$O$_5$ core was seen for the smaller OEC models reported in our previous study.[44] We note that EXAFS data for the NH$_3$-modified OEC have only been reported for samples purified from spinach, not from the cyanobacterial model systems *T. elongatus/vulcanus*, and suggested an elongation of one of the short Mn–Mn distances of 0.02 Å.[113] This type of perturbation is not observed in our optimized Mn$_4$O$_5$Ca–NH$_3$ model. The structural model including both Sr^{2+} and NH$_3$ (Mn$_4$O$_5$Sr–NH$_3$) is found to replicate both effects seen in the singly modified structures.

3.2 Multifrequency EPR and ^{55}Mn-ENDOR of the S$_2$ states of the OEC variants

Multifrequency EPR/^{55}Mn-ENDOR experiments spanning the microwave range from ≈9 to ≈90 GHz were employed to experimentally characterize the electronic structures of the different S$_2$ state forms described above. Fig. 3A (black solid traces) depicts X-band CW EPR spectra of the S$_2$ state of native PSII (Mn$_4$O$_5$Ca),[33] Sr^{2+}-substituted PSII (Mn$_4$O$_5$Sr),[33] NH$_3$-modified (annealed) native PSII (Mn$_4$O$_5$Ca–NH$_3$)[44] and NH$_3$-modified Sr^{2+}-substituted PSII (Mn$_4$O$_5$Sr–NH$_3$). Shown are light-minus-dark spectra, generated by taking the difference between the

illuminated spectrum (S$_2$) and the dark-state spectrum (S$_1$) in order to remove background signals, such as from the cytochromes b_{559} and c_{550}. The modified multiline (Mn$_4$O$_5$Sr, Mn$_4$O$_5$Ca–NH$_3$) displays 26 lines of altered intensity as compared to the native multiline signal with 24 lines. The Mn$_4$O$_5$Sr–NH$_3$ S$_2$ state yields essentially the same modified multiline signal; the simulation superimposing this data trace uses the parameters that fit the Mn$_4$O$_5$Sr dataset.

Fig. 3B shows the corresponding Q-band ESE-detected S$_2$ state multiline EPR signals of the Mn$_4$O$_5$Ca, Mn$_4$O$_5$Sr and Mn$_4$O$_5$Ca–NH$_3$ OEC forms. Pseudo-modulated (CW-like) spectra are shown in order to more clearly visualize differences in the hyperfine structures between the three forms. Compared to earlier published data by Cox *et al.*,[33] the spectra are essentially free of contaminating hexaquo-Mn^{2+} signals. Furthermore, there is a small difference of the centre positions of the multiline spectral envelopes, presumably due to inaccuracy in the micro-wave frequency calibration of this earlier study.

Fig. 3C shows the W-band ESE-detected multiline signals of the Mn$_4$O$_5$Ca, Mn$_4$O$_5$Sr, Mn$_4$O$_5$Ca–NH$_3$ and Mn$_4$O$_5$Ca–NH$_3$ S$_2$ state forms. These spectra do contain small hexaquo-Mn^{2+} contaminations. This contamination manifests itself as six inverted hyperfine lines centred at $g ≈ 2$, as the high-spin Mn^{2+} signal ($S = 5/2$) is over-rotated when using optimal instrumental settings to visualize the $S = 1/2$ multiline signal. No ^{55}Mn hyperfine structure is observable in the W-band multiline EPR spectra. Thus, these signals provide no additional information on the hyperfine matrices. The utility of these high-frequency data instead is to constrain the G tensor. While the spectra of the Mn$_4$O$_5$Ca and the Mn$_4$O$_5$Ca–NH$_3$ cluster show similar signals, centred at $g = 1.975$, the Mn$_4$O$_5$Sr spectrum is shifted to higher field and centred at $g = 1.980$, similar to the shift observed in W-band spectra from the Bittl laboratory.[114] The NH$_3$-modified Sr^{2+}-substituted S$_2$ state signal is centred at $g = 1.979$. The almost identical high-field shift, illustrated by the superimposed Mn$_4$O$_5$Sr simulation, indicates that the G-tensor shift is dependent only on the presence of Sr^{2+} but not NH$_3$. This is in contrast to the result at X-band, which showed that the hyperfine structure is approximately the same for both modifications.

Fig. 3D shows the Q-band Davies ^{55}Mn-ENDOR light-minus-dark spectra, measured at the central magnetic field position of the corresponding EPR spectra (Fig. 3B). The line shape of the ^{55}Mn-ENDOR signal shows only a small field dependence over the 1190 to 1260 mT range (not shown), consistent with its assignment to the tetranuclear Mn cluster.[31] In contrast to the X-band CW EPR spectra described above (Fig. 3A), the S$_2$ states of the native, Sr^{2+}-substituted, NH$_3$-annealed and doubly modified (not shown) OEC give rise to highly similar ^{55}Mn-ENDOR spectra. Five peaks are observed for all three sample types appearing at approximately the same frequency positions and of similar intensities. Small differences in the region of the largest peak (≈115 MHz) may represent residual Mn^{2+} contaminations. Importantly, no large difference is seen with regard to the total spectral breadth of the signal (≈55 to ≈195 MHz). For the NH$_3$-modified S$_2$ state, the results are nominally consistent with the earlier X-band ENDOR data of Peloquin *et al.*[30]
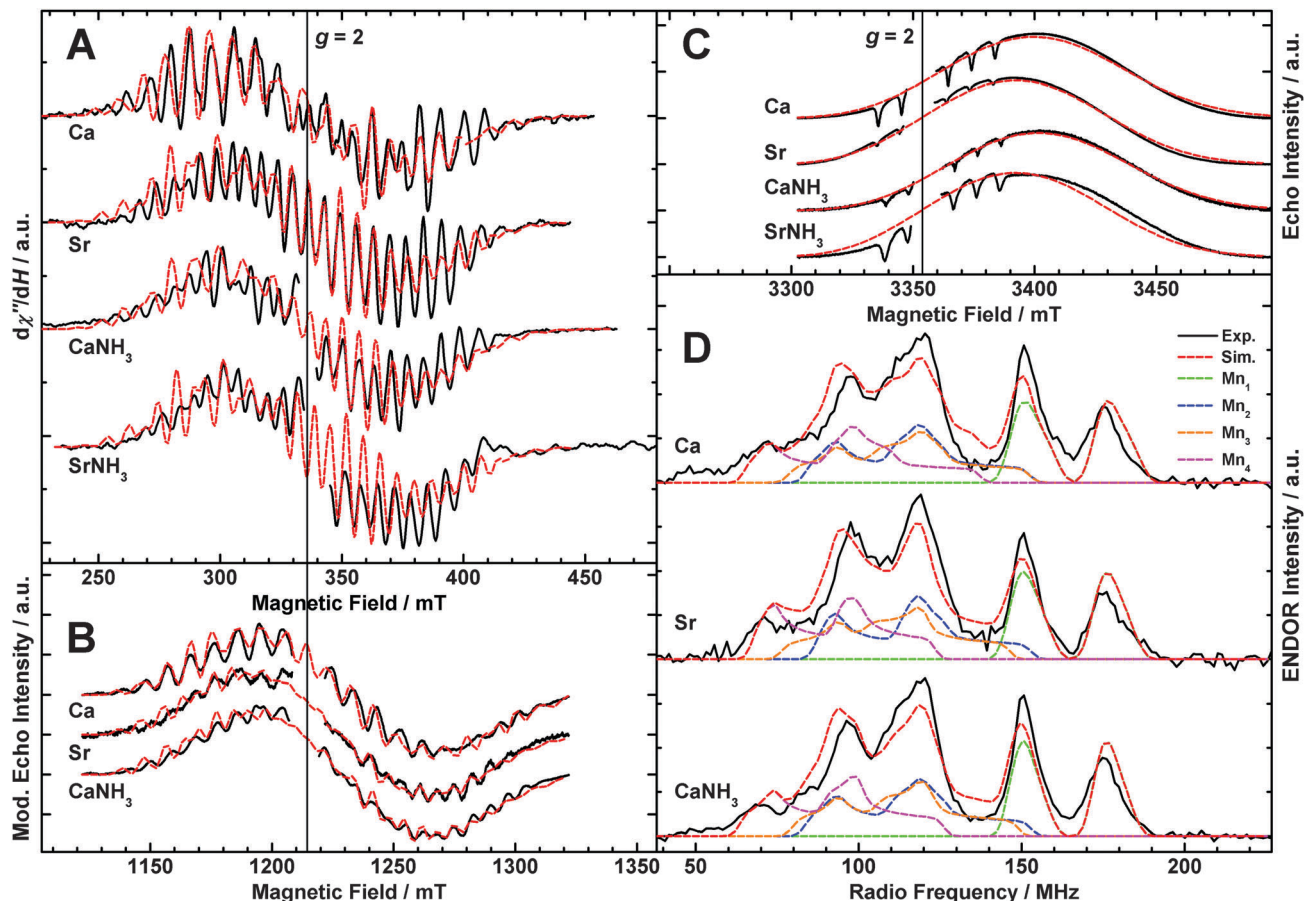
Fig. 3 EPR and ^{55}Mn-ENDOR spectra of the S_2 states of the native (Ca), Sr^{2+}-substituted (Sr), NH_3-modified (CaNH$_3$) and NH_3-modified Sr^{2+}-substituted (SrNH$_3$) OEC in PSII isolated from *T. elongatus*. In panels A, B and D, the black solid traces depict the light-minus-dark subtractions of the experimental spectra. If present, the $g \approx 2$ radical signal of Y$_D$$^\bullet$ (D2-Tyr160) was removed from the EPR spectra for clarity of presentation. Least-squares fittings to the EPR and ^{55}Mn-ENDOR datasets using a model based on the spin Hamiltonian formalism (see Section 2.3 and Sections S3 and S4, ESI†) are represented by superimposing red dashed lines. In panel D, coloured dashed lines represent a decomposition of the simulation showing contributions from the individual ^{55}Mn nuclei. Simulations superimposed on the SrNH$_3$ spectra are those fitted to the Sr dataset. The optimized parameter sets are listed in Table 1. (A) X-band CW EPR. In the Ca and Sr samples, Y$_D$ had been replaced by a phenylalanine, removing the Y$_D$$^\bullet$ signal from the spectra,[112] which were taken from Cox *et al.*[33] The CaNH$_3$ spectrum was originally published in ref. 44. Experimental parameters: microwave frequencies: 9.4097 GHz (Ca), 9.4213 GHz (Sr), 9.4075 GHz (CaNH$_3$), 9.4970 GHz (SrNH$_3$); microwave power: 20 mW; modulation amplitude: 25 G; time constant: 82 ms; temperature: 8.6 K. (B) Q-band ESE-detected EPR. The experimental data are presented as pseudo-modulated, derivative-shaped spectra. Experimental parameters: microwave frequencies: 34.0368 GHz (Ca), 34.0430 GHz (Sr), 34.0162 GHz (CaNH$_3$); shot repetition time: 1 ms; microwave pulse length (π): 24 ns; τ: 260 ns; temperature: 5.2 K. (C) W-band ESE-detected EPR. Contaminating Mn^{2+}, present in the samples in varying concentrations, is evident as over-rotated hyperfine features of negative signal intensity. Experimental parameters: microwave frequencies: 93.9894 GHz (Ca), 93.9781 GHz (Sr), 94.0669 GHz (CaNH$_3$), 94.0615 GHz (SrNH$_3$); shot repetition time: 1 ms (Ca, Sr), 5 ms (CaNH$_3$, SrNH$_3$); microwave pulse length (π): 48 ns; τ: 300 ns; temperature: 4.8 K. (D) Q-band Davies ENDOR. Experimental parameters: microwave frequencies: 33.9678 GHz (Ca), 33.9950 GHz (Sr), 34.0053 GHz (CaNH$_3$); magnetic field: 1220 mT; shot repetition time: 1 ms; microwave pulse length (π): 32 ns; τ: 268 ns; RF pulse length (π_{RF}): 3.5 μs; temperature: 4.8 K.

The Q-band ENDOR spectra presented here do slightly differ from those presented in ref. 33, 34, 44 and 115 with regard to line intensities, discussed in detail in the Section S6 (ESI†).

Spectral simulations of the complete EPR and ^{55}Mn-ENDOR datasets using the spin Hamiltonian formalism are also shown in Fig. 3 (red dashed lines); the fitted effective G and hyperfine tensors A of the Mn clusters in the low-spin S_2 state are listed in Table 1. The effective G tensors of all three spin systems are in the same range as inferred from EPR measurements on PSII single crystals at W-band, *i.e.* $G = [1.997, 1.970, 1.965]$[116] and $G = [1.988, 1.981, 1.965]$.[117] As found previously,[30,31,33,34,44] the inclusion of four hyperfine tensors of approximately the

same magnitude and near-axial symmetry is required to simultaneously fit the X-, Q- and W-band EPR and Q-band ^{55}Mn-ENDOR line widths and shapes. The z component represents the principal component for the fitted G and all four hyperfine tensors. Comparison of the fitted parameters demonstrates that the three samples basically exhibit the same electronic structure. The sets of the four isotropic values $A_{i,\mathrm{iso}}$ deviate only by $\leq 4\%$ between the three different systems and the signs and magnitudes of the anisotropies $A_{i,\mathrm{aniso}}$ are broadly similar, suggesting that there are no significant differences in the electronic exchange coupling schemes of the $Mn_4O_5Ca/Sr(-NH_3)$ clusters.

11882 | *Phys. Chem. Chem. Phys.*, 2014, **16**, 11877–11892

This journal is © the Owner Societies 2014

Table 1 Principal values of the effective G and ^{55}Mn hyperfine tensors A_i for the simulations of the S_2 state spectra of the Mn_4O_5Ca, Mn_4O_5Sr and $Mn_4O_5Ca–NH_3$ clusters in PSII from *T. elongatus*[a]

			A_i/MHz			
		G	A_1	A_2	A_3	A_4
Native	x	1.989	350	214	214	173
	y	1.978	329	195	184	157
	$\perp$ [b]	1.983	339	204	199	165
	z [b]	1.956	321	282	282	251
	iso[c]	1.974	333	230	227	194
	aniso[d]	0.028	19	−78	−83	−87
Sr^{2+}-substituted	x	1.992	328	213	215	161
	y	1.981	347	201	180	175
	$\perp$ [b]	1.986	338	207	197	168
	z [b]	1.963	320	283	270	224
	iso[c]	1.978	332	232	221	187
	aniso[d]	0.024	17	−76	−73	−56
NH_3-modified	x	1.989	326	214	215	154
	y	1.978	345	195	187	175
	$\perp$ [b]	1.984	336	204	201	164
	z [b]	1.956	322	283	275	229
	iso[c]	1.975	331	231	225	186
	aniso[d]	0.027	13	−79	−74	−65

[a] All G and A tensors are collinear. [b] The equatorial and axial G and A_i values are defined as $G_\perp = (G_x + G_y)/2$, $G_\parallel = G_z$, and $A_{i,\perp} = (A_{i,x} + A_{i,y})/2$, $A_{i,\parallel} = A_{i,z}$. [c] The isotropic G and A_i (i = 1–4) values are the averages of the individual values: $G_{iso} = (G_x + G_y + G_z)/3$ and $A_{i,iso} = (A_{i,x} + A_{i,y} + A_{i,z})/3$. [d] The anisotropy in the G and A_i values is expressed as the difference $A_{i,aniso} = A_{i,\perp} − A_{i,\parallel}$.

3.3 Calculated magnetic properties for the native and modified S_2 states of the OEC

The electronic structure of the coupled OEC spin system is defined by the set of six pairwise Mn–Mn exchange interaction terms J_{ij}, which can be calculated using BS-DFT. For all four computational models describing the set of native and chemically perturbed S_2 state clusters, the calculations reveal that the αββα spin configuration (Fig. 4A and B) is the lowest in energy. Sets of J_{ij} coupling constants are given in Table S1 of the ESI.† Diagonalization of the Heisenberg Hamiltonian to obtain the complete spin ladder confirms that all four models exhibit an effective total spin $S_T = 1/2$ ground state, as observed experimentally, and an $S_T = 3/2$ first excited state. The estimated energy differences between the two lowest states of the spin ladder are on the order of 24–26 cm^{-1} for the Mn_4O_5Ca/Sr S_2 state structures, lowering by 7 cm^{-1} upon exchange of W1 for NH_3 (Table S1, ESI†). These values are in the range inferred from experiments.‡ [33,34,118,119]

For all four S_2 state OEC forms, the J-coupling topology consists of three main coupling pathways (Table S1, ESI† and Fig. 4B): (i) an antiferromagnetic coupling pathway between Mn_{D1} and Mn_{C2} (J_{CD}); (ii) a ferromagnetic coupling pathway between Mn_{C2} and Mn_{B3} (J_{BC}); (iii) and an antiferromagnetic

‡ Differences in the experimental numbers between the $Mn_4O_5Ca–NH_3$ (≥ 30 cm^{-1}) and the Mn_4O_5Ca/Sr (≈ 25 cm^{-1}) S_2 states are likely due to different sample types, *i.e.* higher plant *vs.* cyanobacterial PSII with and without EtOH, respectively.
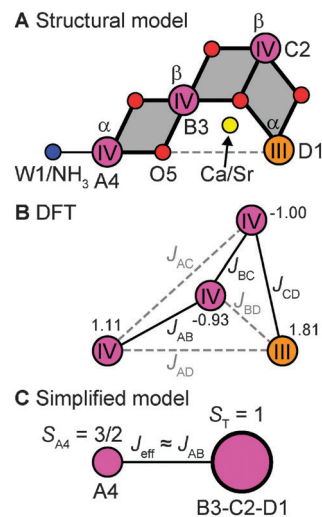

Fig. 4 The magnetism of the low-spin S_2 state. (A) Connectivity of the inorganic centres showing the three μ-oxo-bridged dimanganese units, defining the main electronic exchange pathways of the cluster. (B) Spin coupling scheme showing the main (black solid lines) and weak (grey dashed lines) exchange couplings J_{ij} within the OEC. The numbers next to the Mn ions represent their spin projection factors $\rho_{i,iso}$ for the native S_2 state BS-DFT model. (C) Simplified spin coupling model in which the trimer unit $Mn_{B3}Mn_{C2}Mn_{D1}$ interacts with the outer Mn_{A4} *via* an effective coupling J_{eff} that may be approximated as J_{AB}.

coupling pathway between Mn_{B3} and Mn_{A4} (J_{AB}). The ferromagnetic exchange pathway $J_{BC} = 19–28$ cm^{-1} is the largest in absolute magnitude, while the antiferromagnetic pathways $J_{CD} = −16$ to $−18$ cm^{-1} and $J_{AB} = −12$ to $−16$ cm^{-1} are slightly weaker. The remaining exchange coupling constants J_{AC}, J_{AD} and J_{BD} are small, as can be expected from geometric considerations (see Table S1, ESI†). J_{CD} and J_{BC} represent the two largest exchange interactions within the cuboidal trimer unit ($Mn_{B3}Mn_{C2}Mn_{D1}$) of the cluster, whereas J_{AB} can be considered to a good approximation as being representative of an effective exchange interaction between this cuboidal unit and the outer Mn_{A4}, as shown in Fig. 4C.

Systematic differences are observed for the exchange pathways upon the two chemical perturbations, replacement of Ca^{2+} by Sr^{2+} and NH_3 exchange at W1 (Table S1, ESI†). When comparing the structure pairs that differ in terms of the presence of Ca^{2+} or Sr^{2+}, *i.e.* Mn_4O_5Ca *vs.* Mn_4O_5Sr and $Mn_4O_5Ca–NH_3$ *vs.* $Mn_4O_5Sr–NH_3$, it is seen that only the major coupling pathways J_{CD} and J_{BC} are modified, decreasing by 2 cm^{-1} and 5 cm^{-1}, respectively. J_{AB} remains unchanged. By contrast, for the corresponding structure pairs where NH_3 is exchanged for W1, the J_{CD} pathway is unchanged, while J_{BC} and J_{AB} increase by 4 cm^{-1}. It is noted that the perturbation of the O5 position upon NH_3 substitution, as shown in Fig. 2, results also in an enhancement of J_{BD} by 3 cm^{-1}. In both cases, the changes in the magnetic interactions can be understood within the geometric changes discussed in Section 3.1 (see Fig. 2): Sr^{2+} substitution mostly affects the structure of the cuboidal unit, thus perturbing principally the exchange pathways within the Mn-trimer unit, whereas NH_3 binding perturbs mostly the connectivity between the trimeric moiety and the outer Mn_{A4} (Fig. 4C).

Table 2 Isotropic and anisotropic spin projection factors $\rho_{i,\text{iso}}{}^a$ and $\rho_{i,\text{aniso}}{}^b$, and calculated and experimental isotropic and anisotropic on-site hyperfine values $a_{i,\text{iso}}{}^a$ and $a_{i,\text{aniso}}{}^b$ in MHz for the Mn ions of the BS-DFT models of the Mn_4O_5Ca, Mn_4O_5Sr and $Mn_4O_5Ca–NH_3$ clusters in the low-spin S_2 state configuration^c

Mn ion	Structure	Spin projections		BS-DFT		Experiment	
		$\rho_{i,\text{iso}}$	$\rho_{i,\text{aniso}}$	$a_{i,\text{iso}}$	$a_{i,\text{aniso}}$	$a_{i,\text{iso}}$	$a_{i,\text{aniso}}$
Mn_{A4} (Mn^{IV})	Mn_4O_5Ca	1.11	0.23	−247	−33	−206	25
	Mn_4O_5Sr	1.13	0.19	−247	−32	−204	31
	$Mn_4O_5Ca–NH_3$	0.94	0.36	−242	−30	−245	−9
Mn_{B3} (Mn^{IV})	Mn_4O_5Ca	−0.93	0.29	194	−22	207	26
	Mn_4O_5Sr	−0.92	0.24	194	−21	202	8
	$Mn_4O_5Ca–NH_3$	−0.86	0.44	193	−19	221	−33
Mn_{C2} (Mn^{IV})	Mn_4O_5Ca	−1.00	0.32	212	−17	226	9
	Mn_4O_5Sr	−0.99	0.27	212	−18	224	11
	$Mn_4O_5Ca–NH_3$	−1.01	0.46	213	−16	226	−26
Mn_{D1} (Mn^{III})	Mn_4O_5Ca	1.81	0.38	−128	−142	−186	−46
	Mn_4O_5Sr	1.78	0.32	−138	−144	−188	−41
	$Mn_4O_5Ca–NH_3$	1.92	0.54	−127	−142	−176	−52

^{a} The isotropic $\rho_{i,\text{iso}}$ and $a_{i,\text{iso}}$ values are the averages of the individual tensor components $\rho_{i,\text{iso}} = (2\rho_{i,\perp} + \rho_{i,\parallel})/3$ and $a_{i,\text{iso}} = (a_{i,x} + a_{i,y} + a_{i,z})/3$. ^{b} The anisotropies of the ρ_i and a_i tensors are expressed as the differences $\rho_{i,\text{aniso}} = \rho_{i,\perp} - \rho_{i,\parallel}$ and $a_{i,\text{aniso}} = a_{i,\perp} - a_{i,\parallel}$, i.e. between the perpendicular and parallel tensor components. ^{c} The intrinsic fine structure values of Mn^{IV} ions were assumed to be $d_{A4} = d_{B3} = d_{C2} = 0$ cm^{-1}. For the $Mn_{D1}{}^{III}$ ion, a value of $d_{D1} = -1.43$ cm^{-1} was fitted, with $e_{D1}/d_{D1} = 0$.

Calculated ^{55}Mn on-site (intrinsic/not spin-projected) hyperfine tensors as in the full (non-effective) spin Hamiltonian based on the BS-DFT models are listed in Table 2 for the four S_2 state variants. The calculated isotropic hyperfine values $a_{i,\text{iso}}$ for the three Mn^{IV} ions fall within the range seen in Mn^{IV} model compounds experimentally, i.e. $|a_{\text{iso}}| = 187–253$ MHz (see ref. 30 and 33). The anisotropy of the calculated hyperfine tensors for these three sites is also small, of the order seen in octahedral Mn^{IV} model complexes, i.e. $|a_{\text{aniso}}| < 30$ MHz.[33] For the $Mn_{D1}{}^{III}$ ion, the calculated isotropic hyperfine value (≈ 130 MHz) is smaller than that for Mn^{IV}, as expected, and lies just outside the range seen in Mn^{III} compounds, i.e. $|a_{\text{iso}}| = 165–225$ MHz.[30,33] As typical for Mn^{III}, it exhibits a significant hyperfine anisotropy, more pronounced than for the Mn^{IV} ions. However, it is noted that the calculated values for the $Mn_{D1}{}^{III}$ site are unexpectedly large. Nevertheless, the computed parameters correlate with the inferred site geometry of Mn_{D1}, namely that of a square-pyramidal 5-coordinate Mn^{III} ion. Such a coordination environment generally yields a small isotropic ^{55}Mn on-site hyperfine coupling and a negative anisotropy (see Table 2), consistent with an effective local $^5B_1$ electronic ground state for the $Mn_{D1}{}^{III}$ ion.[30,33,120]

The effective hyperfine couplings measured by EPR spectroscopy for oligonuclear metal complexes reflect the on-site hyperfine couplings of the individual metal ion nuclei scaled by the contribution of the electronic spin of each metal ion to the effective spin state: $A_i = \rho_i a_i$. The set of scaling factors ρ_i, termed spin projection coefficients, are primarily determined by the set of pairwise exchange couplings as detailed in ref. 18,

30, 31, 33, 34, 36, 37 and 63. However, additional terms must be included to correctly estimate such spin projections for the OEC, specifically the relevant on-site fine structure parameters d_i for the individual Mn_i ions,[18,30,33,34,63] yielding what are more accurately described as spin projection tensors. As the coordination geometries of the three Mn^{IV} ions of the S_2 state are all octahedral, their local electronic structure should be of approximate spherical symmetry, their orbitals of t_{2g} origin (d_{xy}, d_{xz} and d_{yz}) being half-filled (local high-spin d^3 configuration). As such, the Mn^{IV} ions are expected to only display small fine structure parameters d_i (< 0.3 cm^{-1})[121] and hence do not need to be explicitly considered. Thus, the set of parameters which define the spin projection tensors in the S_2 state are the six pairwise exchange interaction terms and the fine structure parameter of the Mn^{III} ion, d_{D1}.

Using these spin projection tensors, the fitted projected ^{55}Mn hyperfine tensors were scaled back to on-site hyperfine tensors to allow comparison to the BS-DFT values discussed above (Table 2). The only plausible assignment for all three forms of the OEC is that A_1, A_2, A_3, and A_4 correspond to a_{D1}, a_{A4}, a_{C2} and a_{B3}, respectively. In our previous work,[33] using BS-DFT structural models predating the latest crystal structure,[9] values of -1.2 to -1.3 cm^{-1} were estimated for a supposedly axially symmetric d_{D1} in the native and Sr^{2+}-substituted S_2 states. Using the same approach, d_{D1} was re-estimated. It was possible to obtain on-site hyperfine anisotropies in the ranges characteristic for Mn^{III} and Mn^{IV} ions employing a single value of -1.43 cm^{-1} for the three OEC systems, well within the range typically seen for Mn^{III} model complexes. As discussed above with regard to the hyperfine tensor anisotropy of $Mn_{D1}{}^{III}$, a negative d value requires an effective local $^5B_1$ state for the $Mn_{D1}{}^{III}$ ion and is thus consistent with the square-pyramidal 5-coordinate ligand geometry of $Mn_{D1}{}^{III}$, as present in all computational models. The experimental on-site hyperfine tensor values (Table 2) generally agree well with the BS-DFT estimates and Mn^{III} and Mn^{IV} model compounds, with smaller isotropic values $a_{i,\text{iso}}$ for the Mn^{III} ion than for the Mn^{IV} ions. In the native and Sr^{2+}-substituted models, Mn_{A4} displays a smaller $a_{A4,\text{iso}}$ than computed and in the NH_3-modified system, where it exhibits the largest coupling of the Mn^{IV} ions. Compared to the calculations, the anisotropic components for the Mn^{IV} ions show a larger variance within $|a_{i,\text{aniso}}| \lesssim 30$ MHz. For $Mn_{D1}{}^{III}$, $a_{D1,\text{aniso}} < -40$ MHz is less negative than calculated. Overall, the experimental results confirm that the computed spin coupling schemes serve as a valid description of the native and modified S_2 states.

3.4 The Mn_{D1}–His332-imino-N interaction

Three-pulse ESEEM measurements were performed to characterize the imino-N signal of His332 associated with the OEC variants in the S_2 state. Fig. S4 and S5 (ESI†), respectively, depict τ- and magnetic-field-dependent ($g \approx 2.10$–1.90) light-minus-dark- subtracted spectra and simulations of the native Mn_4O_5Ca (A, B), Sr^{2+}-substituted Mn_4O_5Sr (C, D) and NH_3-modified $Mn_4O_5Ca–NH_3$ (E, F) S_2 state samples. As noted in Pérez Navarro et al.,[44] the ^{14}N nitrogen signal observed for the native S_2 state

11884 | *Phys. Chem. Chem. Phys.*, 2014, **16**, 11877–11892

This journal is © the Owner Societies 2014

from *T. elongatus* is very similar to that measured in PSII from both higher plants (spinach)[122] and the mesophilic cyanobacteria *Synechocystis* sp. PCC 6803,[123] assigned to the imino-N of His332 *via* mutagenesis.[123,124] The signals are essentially the same in the native, Sr^{2+}-substituted and NH_3-modified OEC clusters with regard to both their τ and magnetic-field dependence. The His332 imino-^{14}N signal at Q-band nearly fulfils the cancellation condition, where A_{iso} is twice the ^{14}N nuclear Larmor frequency ($\nu_n = 3.75$ MHz at 1.22 T). The spectra are characterized by three features: the lines centred at frequencies below 2.5 MHz ($\nu_\alpha = \nu_n - |A_{iso}|/2$), single-quantum transitions around 7.5 MHz ($\nu_\beta = \nu_n + |A_{iso}|/2$) and smaller double-quantum resonances around 15 MHz ($\nu_{2\beta} = 2\nu_n + |A_{iso}|$). The line structuring is defined both by the ^{14}N hyperfine anisotropy and the NQI.

HYSCORE spectroscopy (a two-dimensional ESEEM technique) was performed on the three S_2 state OECs at different magnetic-field positions ($g \approx 2.07$–1.93) of the corresponding Q-band EPR envelopes to further constrain the ^{14}N hyperfine and quadrupolar interaction matrices. Panels A, C and E in Fig. 5 show the Fourier-transformed spectra and simulations at the centre field position; low- and high-field spectra and simulations are presented in Fig. S6 and S7 in the ESI.† As seen for the three-pulse ESEEM spectra, their appearance is highly similar for all three variants of the OEC in the S_2 state. In two dimensions, the three features that comprise the Q-band ESEEM spectra appear as cross peaks at corresponding frequencies both in the (−,+) and the (+,+) quadrants. As the ^{14}N hyperfine coupling matches the cancellation condition, the cross peaks are shifted away from the diagonal, instead appearing near the
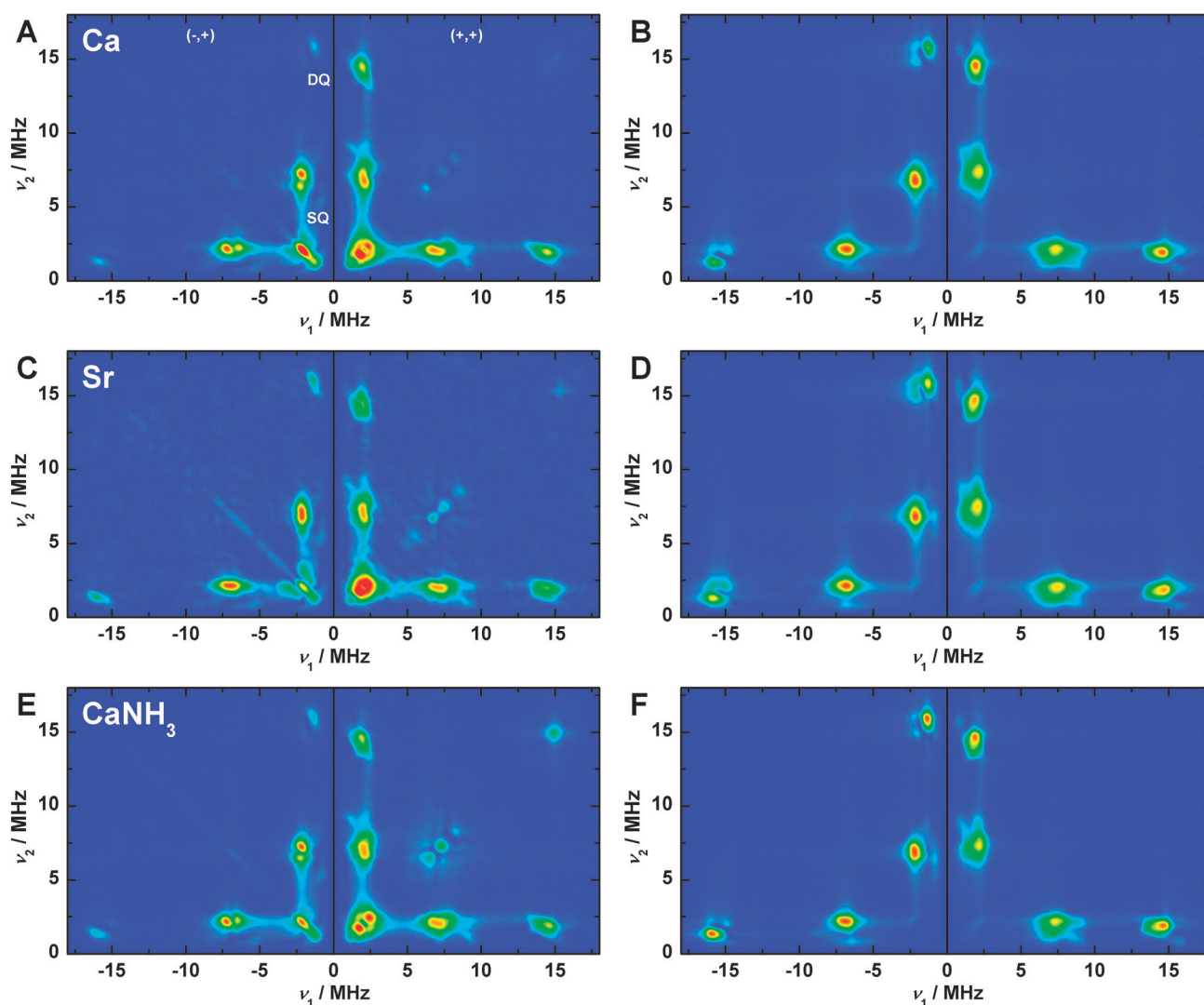

Fig. 5 (−,+) and (+,+) quadrants of the Fourier-transformed Q-band HYSCORE experimental spectra (A, C, E) and spin Hamiltonian-based simulations (B, D, F) of the S_2 state Mn_4O_5Ca (A, B), S_2 state Mn_4O_5Sr (C, D) and annealed S_2 state $Mn_4O_5Ca–NH_3$ (E, F) clusters in PSII samples isolated from *T. elongatus* at central magnetic field. SQ and DQ point out the regions of single- and double-quantum transitions, respectively. The optimized parameter sets for the simulations, as described in Section 2.3 and Sections S3, S4 and S8.4 (ESI†), are listed in Table 3 and, in detail, in Table S2 (ESI†). Experimental parameters: microwave frequencies: 34.0370 GHz (Ca), 34.0433 GHz (Sr), 34.0151 GHz (NH); magnetic fields: 1220 mT (Ca), 1222 mT (NH₃, Sr); shot repetition time: 1 ms; microwave pulse length (π/2): 12 ns; τ: 260 ns; ΔT: 100 ns; temperature: 5.2 K.

frequency axes. Overall, virtually no orientation dependence is seen comparing the spectra at the three different magnetic fields (Section S8.2, ESI†), consistent with the electron–nuclear interaction being dominated by the isotropic component of the hyperfine coupling as compared to the anisotropic part and the traceless NQI, as in ref. 122, 123 and 125. Thus, the orientation of the His332 imino-^{14}N hyperfine tensor relative to the G tensor cannot be determined from this dataset.

Fitted spin Hamiltonian parameters derived from the simultaneous simulation of both the ESEEM and HYSCORE datasets are given in Table 3 together with BS-DFT estimates. To directly compare DFT values with experiment, the calculated site hyperfine tensor for the His332 was multiplied by the axial Mn_{D1} spin projection tensor described in Section 3.3. All DFT models yield virtually the same hyperfine and quadrupole values. The calculated A_{iso} underestimates experimental results by <20%, but the dipolar component A_{dip} and the rhombicity A_η nominally agree with experiment. It is noted that the on-site ^{14}N hyperfine tensor a is expected to be axial with its unique component a_1 aligned along the Mn_{D1}–N bond, as seen in our calculations (Table S2, ESI†). As such, the axial ^{14}N hyperfine component a_1 is essentially rotated 90° relative to that of the Mn_{D1} spin projection tensor, which is expected to coincide with the Jahn–Teller axis of Mn_{D1}^{III}. This 90° rotation explains why the ^{14}N hyperfine tensor A is rhombic in the projected (experimental) reference frame. For a more detailed description of the simulations, see Section S8.4 (ESI†). Importantly, the near-invariance of the imino-N spin Hamiltonian parameters for the three S_2 state forms requires the His332 ligation, the electronic structure of the Mn_{D1}^{III} ion and by extension the whole tetranuclear Mn cluster, to not be significantly perturbed by Ca^{2+}/Sr^{2+} and NH_3/W1 exchange, in line with the EPR/^{55}Mn ENDOR results described in Section 3.2.

While the orientation of the hyperfine tensor relative to the G tensor cannot be determined using ESEEM/HYSCORE at Q-band frequencies, it can be measured at W-band, $e.g.$ using

EDNMR. In our earlier study,[14] it was found that the hyperfine tensor is orientated such that its principal, $i.e.$ the smallest component A_1 is aligned such that it is mid-way between G_x, and G_z. Importantly though, it is noted that the set of spin Hamiltonian parameters deduced from Q-band ESEEM/HYSCORE (Table 3) does not reproduce the W-band data sets (Section S8.3, ESI†). This is not due to the inclusion/exclusion of the NQI term, which, for the W-band EDNMR data, mainly contributes to the spectral line width. To reproduce the field dependence of the ^{14}N- and ^{15}N-EDNMR signals (Fig. S8 and S9, ESI†), the values determined from Q-band ESEEM/HYSCORE needed to be scaled: A_{iso} was decreased by 10%, whereas A_{dip} was increased by a factor of two (Table S2, ESI†). The same results were observed for all three S_2 state forms, which basically exhibit the same ^{14}N-EDNMR spectra. A possible reason for this difference comes from the observation that the ground spin state, an effective spin $S_T = 1/2$ state, is not very well separated energetically from higher spin states in the regime of the W-band excitation energy (≈ 3 cm^{-1}), consistent with DFT estimates for the ground-to-first excited state energy splitting ΔE (Section S7, ESI†). Excited-state mixing due to a small ΔE has the consequence of altering spin Hamiltonian observables such as effective ^{55}Mn and ^{14}N hyperfine tensors. Alternatively, the rhombicity of the effective G tensor as inferred from the EPR/^{55}Mn-ENDOR simulations may be artificial, a consequence of using collinear G and ^{55}Mn hyperfine tensors. This latter suggestion would also explain why the G tensors inferred from W-band measurements on PSII single crystals[116,117] differ from those inferred from our multifrequency measurements on frozen solution PSII samples.

The lack of agreement between the two ^{14}N datasets brings into question whether the W-band ^{14}N/^{15}N-EDNMR signals can be used to assign the exchangeable µ-oxo bridge ^{17}O signal based on the relative orientations of the ^{14}N and ^{17}O hyperfine tensors, as suggested by Rapatskiy $et\ al.$[14] Thus, further experimental results, particularly from single crystals of PSII, are needed to test this proposal (see Section 3.6).

Table 3 Fitted and calculated effective/projected ^{14}N hyperfine and NQI tensors in MHz for the electron–nuclear couplings of the His332 imino-N and of NH_3 with the various cluster forms studied in the S_2 state in PSII from $T.\ elongatus$

S_2 state	^{14}N	Method	$|A_{iso}{}^a|$	$A_{dip}{}^b$	$A_\eta{}^c$	$|e^2Qq/h|$	η^c
Native	His332^d	Exp.	7.1	0.75	0.81	1.97	0.75
		DFT	5.8	0.59	0.74	1.65	0.91
Sr^{2+}-substituted	His332^d	Exp.	7.3	0.69	0.83	1.98	0.79
		DFT	5.8	0.57	0.61	1.65	0.91
NH$_3$-modified	His332^d	Exp.	7.2	0.75	0.89	1.96	0.80
		DFT	6.1	0.71	0.99	1.68	0.88
	NH$_3$	Exp.	2.36	0.33	0.22	1.52	0.47
		DFT	2.68	−0.65	0.02	0.94	0.87
NH$_3$-modified, Sr^{2+}-substituted	NH$_3$	Exp.	2.37	0.28	0.23	1.58	0.45
		DFT	2.68	−0.59	0.03	0.93	0.87

^{a} A_{iso} is defined as the average of the principal components of the hyperfine tensor: $A_{iso} = (A_1 + A_2 + A_3)/3$. ^{b} A_{dip} is defined in terms of T_1, T_2, and T_3 as $A_{dip} = (T_1 + T_2)/2 = -T_3/2$. ^{c} The rhombicity is defined by A_η or $\eta = (T_1 - T_2)/T_3$, respectively. T_1, T_2, and T_3 represent the three principal components of the hyperfine tensors minus A_{iso} and of the NQI tensors and are labelled such that $|T_1| \leq |T_2| \leq |T_3|$. ^{d} The Euler rotation angles $[\alpha,\ \beta,\ \gamma]$ of the NQI relative to the A tensors are $[20, 12, 0]°$, $[18, 9, 0]°$ and $[16, 16, 0]°$ for the Mn_4O_5Ca, Mn_4O_5Sr and $Mn_4O_5Ca–NH_3$ clusters, respectively.

3.5 NH₃ binding to the Ca²⁺- and the Sr²⁺-containing OEC

In the NH_3-modified S_2 state, a second nitrogen nucleus is bound to the Mn cluster as a terminal ligand, as described in Pérez Navarro et al.[44] Its binding can be observed using X-band (three-pulse) ESEEM, as shown in Fig. S11 (ESI†) for $^{14}NH_3/^{15}NH_3$-bound, Ca²⁺- and Sr²⁺-containing PSII. The $^{14}NH_3$ resonances comprise three characteristic single-quantum lines at 0.5, 0.95 and 1.45 MHz split by the NQI and smaller double-quantum transitions centred at 4.9 MHz, highly similar to the higher plant data.[70] Due to the lack of the NQI, the $^{15}NH_3$ signal is clearly less complicated, consisting only of one single-quantum hyperfine peak centred at 0.3 MHz. As seen for the His332 imino-^{14}N signal at Q-band, the NH_3 interaction at X-band fulfils the cancellation condition, leading to a narrow ν_α line while the ν_β line is broadened beyond detection.[70] Most importantly, the spectra of the $^{14}NH_3$-modified Ca²⁺- and Sr²⁺-containing ^{14}N-PSII samples are essentially identical. Thus, NH_3 binding to the Sr²⁺-substituted S_2 state cluster is the same as in the native S_2 state.

In our first report on NH_3 binding to the OEC, only the $^{14}NH_3$ interaction was considered.[44] Here, we simultaneously fit the spectra of both the $^{14}NH_3$-modified ^{15}N-PSII and the $^{15}NH_3$-modified ^{14}N-PSII in the S_2 state (Table 3, Fig. S11 and Table S3, ESI†). This resulted in an optimized hyperfine tensor $A = [2.76\ 2.62\ 1.69]$ MHz for $^{14}NH_3$ (and for ^{15}N scaled by the ratio of the nuclear g values of ^{15}N and ^{14}N) and ^{14}N NQI parameters $e^2Qq/h = 1.52$ MHz and $\eta = 0.47$. Highly similar hyperfine and NQI values reproduce the NH_3 signal observed in the annealed S_2 state of Sr²⁺-containing ^{14}N-PSII. The isotropic ^{14}N hyperfine coupling $A_{iso} = 2.36$ MHz and $A_{dip} = 0.33$ MHz, e^2Qq/h and the asymmetry parameter η are the same as reported before for PSII from *T. elongatus*[44] and similar to the values from the analysis of higher plant X-band ESEEM spectra[70] (Table 3).

An axial projected $^{14}NH_3$ hyperfine tensor is obtained from BS-DFT calculations, as seen in the experiment. This is because (i) the on-site $^{14}NH_3$ hyperfine tensor is axial, and (ii) its axial and equatorial components are essentially coincident with those of the Mn_{A4} spin projection tensor (Table S3, ESI†), unlike the case for the His332 imino-^{14}N a tensor (see Section 3.4). The BS-DFT calculations also reproduce the comparably large and rhombic NQI parameters (Table 3), although the sign of the hyperfine anisotropy is inverted compared to experiment. For more details, see Section S9 in the ESI.†

3.6 Interactions with exchangeable ^{17}O species

As we have recently shown,[14,19] EDNMR spectroscopy at W-band, due to its comparatively high sensitivity, is the preferred method to measure the interactions of exchangeable ^{17}O nuclei with fast-relaxing electronic species such as the S_2 state of the OEC. Fig. 6 shows these spectra and simulations (see Section 2.3 and Sections S3 and S4, ESI† for details) of the single-quantum region for the native, the Sr²⁺-substituted, the NH_3-annealed and the Sr²⁺- and NH_3-modified S_2 state variants after $H_2^{17}O$ buffer exchange in the S_1 state (see Fig. S12 (ESI†) for the double-quantum region). The spectrum of the native system exhibits the single- and double-quantum resonances of the
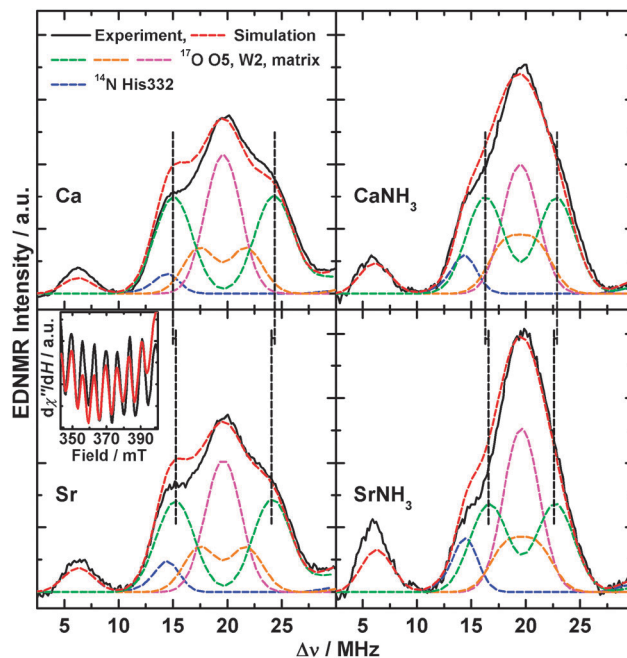

Fig. 6 ^{17}O-EDNMR spectra of the native (Ca) the Sr²⁺-substituted (Sr), the NH_3-annealed (CaNH₃) and the Sr²⁺-substituted NH_3-annealed (SrNH₃) S_2 states in PSII samples isolated from *T. elongatus*. Black solid traces depict the single-quantum region of background-corrected experimental spectra; superimposing red dashed traces represent simulations based on the spin Hamiltonian formalism as outlined in Section 2.3 and Sections S3 and S4 (ESI†). Coloured dashed lines represent a decomposition of the simulation showing contributions from the individual ^{14}N and ^{17}O nuclei. Black dashed lines highlight the decrease of the strong ^{17}O interaction upon Ca²⁺/Sr²⁺ exchange. The optimized parameter sets are listed in Table S4 (ESI†). Double-quantum regions are shown in Fig. S12 (ESI†). Inset: a section of the X-band CW EPR spectra of the Sr²⁺-substituted S_2 state in PSII samples in the absence (black) and presence (red) of $H_2^{17}O$ showing no line broadening upon ^{17}O exchange. Experimental parameters: see Fig. S12 and for the inset Fig. S14 (ESI†).

imino-^{14}N of His332 (blue) and of three different classes of ^{17}O species,[14] i.e. (i) a strongly coupled, bridging species (green), (ii) an intermediately coupled terminal O-ligand (orange), and (iii) a weakly coupled terminal class (cyan). These were assigned to the μ-oxo bridge O5, the hydroxide ion W2[12] and the H_2O matrix (comprising ligand W1 of Mn_{A4} and two H_2O ligands at the Ca²⁺ ion), respectively. NH_3 binding causes a narrowing of the ^{17}O single- and double-quantum envelopes, reproduced by a decrease of the hyperfine couplings of O5 and W2 and concomitant reduction of the matrix line intensity, which was interpreted by NH_3 binding to Mn_{A4} in exchange for W1.[44] Comparing these two spectral forms to those of the corresponding Sr²⁺-substituted W1- and NH_3-containing clusters (Fig. S13, ESI†), we see a systematic narrowing of the single-quantum envelope by ≈ 0.5 MHz and a corresponding narrowing of the double-quantum envelope. This can be reproduced by spectral simulations in which the hyperfine couplings of the μ-oxo bridge are reduced accordingly (W1: 9.2 MHz vs. 9.7 MHz, NH_3: 6.5 vs. 7.0 MHz), while the other ^{17}O interactions remain unaltered (for a complete set of hyperfine parameters, see Table S4, ESI†). Although weaker than the NH_3 effect, the

This journal is © the Owner Societies 2014

Phys. Chem. Chem. Phys., 2014, **16**, 11877–11892 | **11887**

narrowing was found to be reproducible in all Sr^{2+}-substituted PSII samples. It clearly shows that Ca^{2+}/Sr^{2+} exchange perturbs the μ-oxo bridge, in addition to a simultaneous modification by NH_3 binding.

The inset in Fig. 6 depicts a section of the X-Band CW EPR spectra of the Sr^{2+}-substituted S_2 state, which exhibits an intrinsically smaller average line width (≈ 3.6 mT peak-to-peak) than the native form (≈ 4 mT), in the presence and absence of ^{17}O (see Fig. S14 (ESI†) for the entire spectra). No EPR line broadening is observed upon ^{17}O exchange. This demonstrates that the largest ^{17}O coupling represents only one exchangeable oxo bridge. In the case of two hyperfine interactions of ≈ 10 MHz, the effective line broadening due to the combined ^{17}O couplings would be larger than 120 MHz or 4.3 mT, exceeding the actual line width.

4 Discussion

4.1 A common electronic structure of the S_2 state variants

Our DFT results show that the Sr^{2+}-substituted, the NH_3-annealed and the Sr^{2+}- and NH_3-modified low-spin S_2 states basically represent the same structure on both a geometric and electronic level. This result is not immediately obvious from their X-band EPR signals. Indeed historically, the Sr^{2+}-substituted and NH_3-modified forms were explained in terms of a change of the valence state distribution within the Mn tetramer and thus of the coordination environment of the Mn^{III} ion.[126] The comprehensive approach pursued in this study conclusively rules out such a mechanism for electronic structure perturbation. Instead, as proposed by our group,[33,34,63] multiline heterogeneity reflects rather subtle changes of the Mn-tetramer structure. The similarity of the perturbed multiline forms suggest a common mechanism for electronic perturbation, which probably also explains S_1 state heterogeneity. This is discussed below, with reference to solvent access, substrate binding and exchange.

4.1.1 The mechanism of structural perturbation.
In Su *et al.*,[34] a qualitative model for multiline heterogeneity was proposed. In this model, the electronic structure of the S_2 state was considered in terms of a simplified model of two spin fragments: (i) a cuboidal trimer unit, made up of Mn_{D1}, Mn_{C2} and Mn_{B3}, and (ii) a 'monomeric' Mn unit, consisting of the outer Mn_{A4}. Therein, variation of the electronic structure in S_2 was attributed to changes in the connectivity of the outer Mn_{A4} to the cuboid, changing the properties of the electronic ground state by altering the mixing-in of excited spin state character. The physical rationale for this observation was that the outer Mn_{A4} represents the solvent accessible end of the cluster. It has two water-derived ligands and solvent channels that begin or terminate at this site.[9,127] As such, it is this site and its connection to the rest of the cluster that is most likely to vary amongst different sample conditions and possibly different PSII species. In terms of this 'monomer–trimer' model with regard to the two modifications discussed here, Ca^{2+}/Sr^{2+} forms part of the linkage between the cuboidal and outer fragments, as mediated by the μ-oxo bridge O5, whereas NH_3 binds to the

outer Mn_{A4}, also perturbing O5, the bridge *trans* to its binding position W1.[44]

The magnetic observable that is altered upon Ca^{2+}/Sr^{2+} replacement and/or $W1/NH_3$ exchange, leading to the perturbed multiline forms is the ^{55}Mn hyperfine anisotropy. Small perturbations of the four hyperfine tensors result in a change in the hyperfine peak superposition, altering the apparent structure of the X-band EPR signal (Fig. 3A). Importantly these changes are subtle, as demonstrated by the invariance of the ^{55}Mn-ENDOR spectra (Fig. 3D). The ^{55}Mn hyperfine anisotropy is not a site property, but instead an indirect measure of the fine structure splitting of the Mn^{III} ion[30,33,34,63] or, in the 'monomer–trimer' model, the zero-field splitting of the whole trimer unit. Within this model, its contribution is modulated by the electronic connectivity between the two fragments, predominantly the exchange pathway J_{AB}, the coupling that mostly defines the energy splitting ΔE between the ground state and the first excited state (Fig. 4C). Our BS-DFT results support this basic mechanism for electronic structure perturbation and, for the first time, describe the changes on the molecular level that impart this variation, and which differ for the two modifications. Upon replacement of Ca^{2+} by Sr^{2+}, the slight distortion of the cuboidal moiety leads to a perturbation of the intra-cuboidal exchange network and possibly the Mn_{D1}^{III} site fine structure splitting. It is noted that this, besides changing the ^{55}Mn hyperfine anisotropy, also manifests itself in terms of the G tensor, also contributing to the altered multiline appearance and the g shift of the W-band EPR signal. Exchange of W1 by NH_3 affects the connectivity of the outer Mn_{A4} to the cuboidal unit, as modulated by the μ-oxo bridge O5, perturbing the J_{AB} exchange pathway, thus changing the ^{55}Mn hyperfine anisotropy. In the case of the S_2 state variant that contains both these modifications, their effects on the electronic structure are additive. It is noted that it is the properties of the cuboidal unit that define the G tensor as opposed to the outer Mn_{A4}, which presumably has an isotropic on-site g value. This is expected, as it is the Mn_{D1}^{III} ion, which is part of the trimer fragment in the $S = 1/2$ configuration, that should form the dominant contribution to the anisotropy of the G tensor in all four systems.

4.1.2 The Mn_{D1}–His332-imino-N and Mn_{A4}–NH_3 interactions as local probes for the electronic structure

4.1.2a The Mn_{D1}–His332-imino-N interaction. As described by Stich *et al.*,[123] the magnitude of the Mn_{D1}–His332 imino-N hyperfine interaction, as compared against mixed-valence $Mn^{III}Mn^{IV}$ model compounds and protein cofactors with imidazole ligands to Mn^{III} ($A_{iso} \leq 13$ MHz) and Mn^{IV} ions ($A_{iso} = 1.5–3.3$ MHz),[128–134] favours assigning Mn_{D1} as the only Mn^{III} ion of the S_2 state, consistent with the EPR/^{55}Mn-ENDOR/DFT results already reported in the literature and detailed above (Sections 3.1–3.3). The large hyperfine couplings seen for ligands coordinating to Mn^{III} in S_2 (and model systems) comes from the fact that the Mn^{III} ion carries the largest spin projection coefficient, *i.e.* in Mn dimers $\rho_{iso}(Mn^{III}) = 2$ and $\rho_{iso}(Mn^{IV}) = -1$. Interestingly, the hyperfine and quadrupole couplings of imidazole ligands of Mn^{III} ions differ depending on whether they represent axial ($A_{iso} = 9–13$ MHz, $e^2Qq/h = 2.1–3.0$ MHz)[128–132] or equatorial ligands ($A_{iso} = 1.5–6.6$ MHz, $e^2Qq/h = 1.5–2.5$ MHz).[131–134] The values seen for the His332

11888 | *Phys. Chem. Chem. Phys.*, 2014, **16**, 11877–11892

This journal is © the Owner Societies 2014

imino-N (A_{iso} = 7.1 MHz, e^2Qq/h = 1.97 MHz) fall closer to the equatorial range supporting its assignment as an equatorial ligand consistent with DFT structural models. In such models,[12,37,40,103,106] the local Jahn–Teller axis of the Mn_{D1}^{III} ion is aligned along the open coordination site, thus considered a pseudo-Jahn–Teller axis, perpendicular to the Mn_{D1}–N bond. It is supposed that the reason why the ^{14}N couplings measured for the His332 do not exactly fall within the range seen in model complexes is that all model complexes measured thus far represent 6-coordinate Mn^{III} ions whereas the Mn_{D1}^{III} ion in the S_2 state is 5-coordinate.

4.1.2b The Mn_{A4}–NH_3 interaction. As recently shown in Pérez Navarro *et al.*,[44] the binding site of NH_3 is likely the W1 site. The small effective isotropic ^{14}N hyperfine coupling (A_{iso} = 2.36 MHz) and the axiality of the hyperfine tensor are both consistent with a terminal ligand to a Mn^{IV} (d^3) ion.[44,70] The similar A_{iso} in the Mn_4O_5Sr–NH_3 cluster confirms that the oxidation state of the Mn_{A4} ion is not altered by Sr^{2+} substitution. Moreover, the binding mode and perturbation mechanism of NH_3 is the same in the Ca^{2+}- and Sr^{2+}-containing Mn clusters. The non-axiality of the electric field gradient (η = 0.47) is characteristic for this ligand. A large asymmetry parameter is uncommon for a terminal ligand of Mn^{IV} (although our value is already $\approx$20% smaller than that reported earlier[70]). The latest crystal structure[9] suggests that such an asymmetric distortion could be present for the W1 site due to the charged residue D1-Asp61, in H-bonding distance to W1/NH_3, as seen for other protein systems.[135] Indeed, upon inclusion of the Asp61 residue, which was not included in our previous, smaller BS-DFT model,[44] the asymmetric quadrupole tensor is now reproduced, and the hyperfine coupling constant shows better agreement with experiment (Fig. 7 and Table 3). In contrast, such an asymmetric distortion is not seen for the W2 ligand as a similar charged amino-acid residue partner is not present to provide a H-bond.

4.2 The exchangeable μ-oxo bridge

Both modifications investigated, Ca^{2+}/Sr^{2+} substitution and NH_3/W1 replacement, perturb the ^{17}O-EDNMR signals of exchangeable oxygen species of the OEC, specifically the exchangeable μ-oxo bridge. It is this bridge that likely represents one of the substrate water sites of the Mn tetramer. As the electronic structure of the OEC is essentially invariant for all four OEC forms, the change in hyperfine coupling for this μ-oxo bridge must represent a site modification, near or at the oxygen nucleus. NH_3 binding primarily affects the connectivity of the outer Mn_{A4} to the cuboidal trimer, whereas Sr^{2+} substitution instead perturbs the exchange network within the cluster. Thus, it can be surmised that the exchangeable μ-oxo bridge must both coordinate to the outer Mn_{A4} and be associated with the Ca^{2+}/Sr^{2+} ion itself as a structural element of the cuboidal trimer. Only the bridge O5 fulfils both these criteria. As a ligand to the Ca^{2+}/Sr^{2+} ion, O5 is affected by the exchange of these ions of the same charge but different sizes. Similarly, as argued in Pérez Navarro *et al.*,[44] NH_3/W1 exchange perturbs O5 by binding *trans* to this bridge position, distorting the Mn_{A4}–O5 bond length.

It is noted that these results exclude the possibility that NH_3 displaces the exchangeable μ-oxo bridge as a bridging –NH_2– species, an alternative rationale for the narrowing of the [17]O signal envelope in line with earlier suggestions.[70] Ca^{2+}/Sr^{2+} and W1/NH_3 exchange are *additive* in terms of their effect on the width of the ^{17}O-EDNMR envelope, modelled here as defined by the μ-oxo bridge hyperfine coupling A_{iso}. This result mirrors the structural modifications observed for the doubly modified Mn_4O_5Sr–NH_3 OEC model; *i.e.*, the model contains *additive* structural modifications reflecting both singularly modified Mn_4O_5Sr and Mn_4O_5Ca–NH_3 structures. If instead the NH_3 did indeed replace the bridge, the width of the ^{17}O-EDNMR envelope would be now defined by the W2 hyperfine coupling, and as such should be invariant to Ca^{2+}/Sr^{2+} substitution. It is also noted that NH_3 replacement of the exchangeable bridge O5 cannot quantitatively explain the virtually unaltered [14]NH_3 signal upon exchange of the O5-binding Ca^{2+}, and the [17]O hyperfine changes. Assuming an unaltered spin density on the bridge position, as follows from the similar spin projection factors for the four Mn ions, the measured ^{14}N hyperfine coupling for the bound ammonia at this position is far too small. On the other hand, the [17]O coupling of 6.5–7 MHz seen for the NH_3/W1-exchanged system is in the range of those observed in Mn model complexes with a N-ligand *trans* to the oxo bridge.[14]

5 Conclusions

Time-dependent mass spectrometry experiments indicate that the early binding substrate (W_S) is associated with all intermediate states of the OEC.[66,136] Furthermore, the relatively slow exchange and the S-state dependence of this bound substrate with bulk water suggests that it represents a ligand of (a) Mn ion(s). As Ca^{2+}/Sr^{2+} substitution also perturbs its exchange rate, W_S is also supposed to coordinate to the Ca^{2+} ion.[65,66] Of the exchangeable oxygen species identified here by ^{17}O-EDNMR, only O5 is a ligand to both Mn and Ca^{2+}. Similarly, only the O5 spectral signature is perturbed by Ca^{2+}/Sr^{2+} exchange. Thus, O5 is the most likely candidate for W_S. This assignment limits the
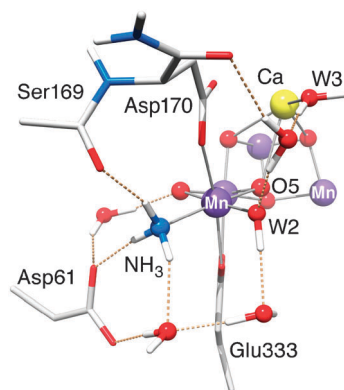

Fig. 7 Hydrogen bonding network in the vicinity of the Mn_{A4}-bound NH_3, as observed in the optimized DFT structure of the Mn_4O_5Ca–NH_3 model. Mn ions are depicted in purple, O in red, Ca in yellow, C in light grey, N in blue and H in white. Only relevant residues, water molecules and protons are shown.

This journal is © the Owner Societies 2014

Phys. Chem. Chem. Phys., 2014, **16**, 11877–11892 | **11889**

possible reaction pathways for photosynthetic water splitting, and lays a foundation for studies of higher oxidized S states, which will serve to identify the second, fast exchanging substrate and eventually elucidate the mechanism of O–O bond formation. Currently two pathways are envisaged: O–O bond formation could proceed as a coupling between O5 and either (i) Mn_{A4}-bound W2 or Ca^{2+}-bound W3, or (ii) a further oxygen not present yet in the S_2 state.

Acknowledgements

Notes and references

1 P. Joliot, G. Barbieri and R. Chabaud, *Photochem. Photobiol.*, 1969, **10**, 309–329.

2 B. Kok, B. Forbush and M. McGloin, *Photochem. Photobiol.*, 1970, **11**, 457–475.

3 J. P. McEvoy and G. W. Brudvig, *Chem. Rev.*, 2006, **106**, 4455–4483.

4 W. Lubitz, E. J. Reijerse and J. Messinger, *Energy Environ. Sci.*, 2008, **1**, 15–31.

5 J. Messinger, T. Noguchi and J. Yano, in *Molecular Solar Fuels*, ed. T. J. Wydrzynski and W. Hillier, Royal Society of Chemistry, Cambridge, 2012, pp. 163–207.

6 N. Cox and W. Lubitz, in *Chemical Energy Storage*, ed. R. Schlögl, De Gruyter Publishers, Berlin, 2012, pp. 185–224.

7 N. Cox and J. Messinger, *Biochim. Biophys. Acta, Bioenerg.*, 2013, **1827**, 1020–1030.

8 N. Cox, D. A. Pantazis, F. Neese and W. Lubitz, *Acc. Chem. Res.*, 2013, **46**, 1588–1596.

9 Y. Umena, K. Kawakami, J.-R. Shen and N. Kamiya, *Nature*, 2011, **473**, 55–60.

10 C. P. Aznar and R. D. Britt, *Philos. Trans. R. Soc. London, Ser. B*, 2002, **357**, 1359–1365.

11 K. A. Åhrling, M. C. W. Evans, J. H. A. Nugent, R. J. Ball and R. J. Pace, *Biochemistry*, 2006, **45**, 7069–7082.

12 W. Ames, D. A. Pantazis, V. Krewald, N. Cox, J. Messinger, W. Lubitz and F. Neese, *J. Am. Chem. Soc.*, 2011, **133**, 19743–19757.

13 S. Milikisiyants, R. Chatterjee, C. S. Coates, F. H. M. Koua, J.-R. Shen and K. V. Lakshmi, *Energy Environ. Sci.*, 2012, **5**, 7747–7756.

14 L. Rapatskiy, N. Cox, A. Savitsky, W. M. Ames, J. Sander, M. M. Nowaczyk, M. Rögner, A. Boussac, F. Neese, J. Messinger and W. Lubitz, *J. Am. Chem. Soc.*, 2012, **134**, 16619–16634.

15 H. Nagashima and H. Mino, *Biochim. Biophys. Acta, Bioenerg.*, 2013, **1827**, 1165–1173.

16 A. Haddy, *Photosynth. Res.*, 2007, **92**, 357–368.

17 L. Kulik and W. Lubitz, *Photosynth. Res.*, 2009, **102**, 391–401.

18 T. Lohmiller, W. Ames, W. Lubitz, N. Cox and S. K. Misra, *Appl. Magn. Reson.*, 2013, **44**, 691–720.

19 N. Cox, W. Lubitz and A. Savitsky, *Mol. Phys.*, 2013, **111**, 2788–2808.

20 J. L. Casey and K. Sauer, *Biochim. Biophys. Acta, Bioenerg.*, 1984, **767**, 21–28.

21 J. C. de Paula and G. W. Brudvig, *J. Am. Chem. Soc.*, 1985, **107**, 2643–2648.

22 K. A. Åhrling, M. C. Evans, J. H. Nugent and R. J. Pace, *Biochim. Biophys. Acta, Bioenerg.*, 2004, **1656**, 66–77.

23 G. C. Dismukes and Y. Siderer, *Proc. Natl. Acad. Sci. U. S. A.*, 1981, **78**, 274–278.

24 A. Boussac, S. Un, O. Horner and A. W. Rutherford, *Biochemistry*, 1998, **37**, 4001–4007.

25 A. Boussac, H. Kuhl, S. Un, M. Rögner and A. W. Rutherford, *Biochemistry*, 1998, **37**, 8995–9000.

26 O. Horner, E. Rivière, G. Blondin, S. Un, A. W. Rutherford, J.-J. Girerd and A. Boussac, *J. Am. Chem. Soc.*, 1998, **120**, 7924–7928.

27 A. Boussac and A. W. Rutherford, *Biochim. Biophys. Acta, Bioenerg.*, 2000, **1457**, 145–156.

28 A. Haddy, K. V. Lakshmi, G. W. Brudvig and H. A. Frank, *Biophys. J.*, 2004, **87**, 2885–2896.

29 A. Boussac, J. J. Girerd and A. W. Rutherford, *Biochemistry*, 1996, **35**, 6984–6989.

30 J. M. Peloquin, K. A. Campbell, D. W. Randall, M. A. Evanchik, V. L. Pecoraro, W. H. Armstrong and R. D. Britt, *J. Am. Chem. Soc.*, 2000, **122**, 10926–10942.

31 L. V. Kulik, B. Epel, W. Lubitz and J. Messinger, *J. Am. Chem. Soc.*, 2007, **129**, 13421–13435.

32 C. Teutloff, S. Pudollek, S. Kessen, M. Broser, A. Zouni and R. Bittl, *Phys. Chem. Chem. Phys.*, 2009, **11**, 6715–6726.

33 N. Cox, L. Rapatskiy, J.-H. Su, D. A. Pantazis, M. Sugiura, L. Kulik, P. Dorlet, A. W. Rutherford, F. Neese, A. Boussac, W. Lubitz and J. Messinger, *J. Am. Chem. Soc.*, 2011, **133**, 3635–3648.

34 J.-H. Su, N. Cox, W. Ames, D. A. Pantazis, L. Rapatskiy, T. Lohmiller, L. V. Kulik, P. Dorlet, A. W. Rutherford, F. Neese, A. Boussac, W. Lubitz and J. Messinger, *Biochim. Biophys. Acta, Bioenerg.*, 2011, **1807**, 829–840.

35 F. Neese, *Coord. Chem. Rev.*, 2009, **253**, 526–563.

36 D. A. Pantazis, M. Orio, T. Petrenko, S. Zein, E. Bill, W. Lubitz, J. Messinger and F. Neese, *Chem.–Eur. J.*, 2009, **15**, 5108–5123.

37 D. A. Pantazis, M. Orio, T. Petrenko, S. Zein, W. Lubitz, J. Messinger and F. Neese, *Phys. Chem. Chem. Phys.*, 2009, **11**, 6788–6798.

38 S. Schinzel, J. Schraut, A. Arbuznikov, P. Siegbahn and M. Kaupp, *Chem.–Eur. J.*, 2010, **16**, 10424–10438.

39 N. Cox, W. Ames, B. Epel, L. V. Kulik, L. Rapatskiy, F. Neese, J. Messinger, K. Wieghardt and W. Lubitz, *Inorg. Chem.*, 2011, **50**, 8238–8251.

40 D. A. Pantazis, W. Ames, N. Cox, W. Lubitz and F. Neese, *Angew. Chem., Int. Ed.*, 2012, **51**, 9935–9940.

41 H. Isobe, M. Shoji, S. Yamanaka, Y. Umena, K. Kawakami, N. Kamiya, J.-R. Shen and K. Yamaguchi, *Dalton Trans.*, 2012, **41**, 13727–13740.

42 K. Yamaguchi, H. Isobe, S. Yamanaka, T. Saito, K. Kanda, M. Shoji, Y. Umena, K. Kawakami, J.-R. Shen, N. Kamiya and M. Okumura, *Int. J. Quantum Chem.*, 2013, **113**, 525–541.

43 V. Krewald, F. Neese and D. A. Pantazis, *J. Am. Chem. Soc.*, 2013, **135**, 5726–5739.

44 M. Pérez Navarro, W. M. Ames, H. Nilsson, T. Lohmiller, D. A. Pantazis, L. Rapatskiy, M. M. Nowaczyk, F. Neese, A. Boussac, J. Messinger, W. Lubitz and N. Cox, *Proc. Natl. Acad. Sci. U. S. A.*, 2013, **110**, 15561–15566.

45 A. Boussac and A. W. Rutherford, *Biochemistry*, 1988, **27**, 3476–3483.

46 T. A. Ono and Y. Inoue, *Arch. Biochem. Biophys.*, 1989, **275**, 440–448.

47 A. Boussac, F. Rappaport, P. Carrier, J. M. Verbavatz, R. Gobin, D. Kirilovsky, A. W. Rutherford and M. Sugiura, *J. Biol. Chem.*, 2004, **279**, 22809–22819.

48 W. F. Beck, J. C. de Paula and G. W. Brudvig, *J. Am. Chem. Soc.*, 1986, **108**, 4018–4022.

49 W. F. Beck and G. W. Brudvig, *Biochemistry*, 1986, **25**, 6479–6486.

50 L.-E. Andréasson, Ö. Hansson and K. von Schenck, *Biochim. Biophys. Acta, Bioenerg.*, 1988, **936**, 351–360.

51 A. Boussac, A. W. Rutherford and S. Styring, *Biochemistry*, 1990, **29**, 24–32.

52 D. H. Kim, R. D. Britt, M. P. Klein and K. Sauer, *J. Am. Chem. Soc.*, 1990, **112**, 9389–9391.

53 D. H. Kim, R. D. Britt, M. P. Klein and K. Sauer, *Biochemistry*, 1992, **31**, 541–547.

54 A. Boussac, M. Sugiura, Y. Inoue and A. W. Rutherford, *Biochemistry*, 2000, **39**, 13788–13799.

55 M. C. W. Evans, R. J. Ball and J. H. A. Nugent, *FEBS Lett.*, 2005, **579**, 3081–3084.

56 D. F. Ghanotakis, G. T. Babcock and C. F. Yocum, *FEBS Lett.*, 1984, **167**, 127–130.

57 P. O. Sandusky and C. F. Yocum, *Biochim. Biophys. Acta*, 1984, **766**, 603–611.

58 P. O. Sandusky and C. F. Yocum, *Biochim. Biophys. Acta*, 1986, **849**, 85–93.

59 T.-a. Ono and Y. Inoue, *FEBS Lett.*, 1988, **227**, 147–152.

60 A. Boussac, J. L. Zimmermann and A. W. Rutherford, *Biochemistry*, 1989, **28**, 8984–8989.

61 M. Sivaraja, J. Tso and G. C. Dismukes, *Biochemistry*, 1989, **28**, 9459–9464.

62 A. Boussac, J. L. Zimmermann, A. W. Rutherford and J. Lavergne, *Nature*, 1990, **347**, 303–306.

63 T. Lohmiller, N. Cox, J.-H. Su, J. Messinger and W. Lubitz, *J. Biol. Chem.*, 2012, **287**, 24721–24733.

64 J. S. Vrettos, D. A. Stone and G. W. Brudvig, *Biochemistry*, 2001, **40**, 7937–7945.

65 G. Hendry and T. Wydrzynski, *Biochemistry*, 2003, **42**, 6209–6217.

66 W. Hillier and T. Wydrzynski, *Coord. Chem. Rev.*, 2008, **252**, 306–317.

67 J. Messinger, M. Badger and T. Wydrzynski, *Proc. Natl. Acad. Sci. U. S. A.*, 1995, **92**, 3209–3213.

68 K. Beckmann, J. Messinger, M. R. Badger, T. Wydrzynski and W. Hillier, *Photosynth. Res.*, 2009, **102**, 511–522.

69 B. A. Diner and R. D. Britt, in *Photosystem II: The Light-Driven Water:Plastoquinone Oxidoreductase*, ed. T. Wydrzynski and K. Satoh, Springer, Dordrecht, 2005, vol. 1, pp. 207–233.

70 R. D. Britt, J. L. Zimmermann, K. Sauer and M. P. Klein, *J. Am. Chem. Soc.*, 1989, **111**, 3522–3532.

71 M. Tsuno, H. Suzuki, T. Kondo, H. Mino and T. Noguchi, *Biochemistry*, 2011, **50**, 2506–2514.

72 M. Sugiura, A. Boussac, T. Noguchi and F. Rappaport, *Biochim. Biophys. Acta, Bioenerg.*, 2008, **1777**, 331–342.

73 N. Ishida, M. Sugiura, F. Rappaport, T. L. Lai, A. W. Rutherford and A. Boussac, *J. Biol. Chem.*, 2008, **283**, 13330–13340.

74 J. Sander, M. Nowaczyk, J. Buchta, H. Dau, I. Vass, Z. Deák, M. Dorogi, M. Iwai and M. Rögner, *J. Biol. Chem.*, 2010, **285**, 29851–29856.

75 M. M. Nowaczyk, K. Krause, M. Mieseler, A. Sczibilanski, M. Ikeuchi and M. Rögner, *Biochim. Biophys. Acta, Bioenerg.*, 2012, **1817**, 1339–1345.

76 E. Reijerse, F. Lendzian, R. Isaacson and W. Lubitz, *J. Magn. Reson.*, 2012, **214**, 237–243.

77 E. L. Hahn, *Phys. Rev.*, 1950, **80**, 580–594.

78 L. G. Rowan, E. L. Hahn and W. B. Mims, *Phys. Rev.*, 1965, **137**, A61–A71.

79 P. Höfer, A. Grupp, H. Nebenführ and M. Mehring, *Chem. Phys. Lett.*, 1986, **132**, 279–282.

80 E. R. Davies, *Phys. Lett. A*, 1974, **A47**, 1–2.

81 P. Schosseler, T. Wacker and A. Schweiger, *Chem. Phys. Lett.*, 1994, **224**, 319–324.

82 S. Stoll and A. Schweiger, *J. Magn. Reson.*, 2006, **178**, 42–55.

83 F. Neese, *Wiley Interdisc. Rev.: Comput. Mol. Sci.*, 2012, **2**, 73–78.

84 J. P. Perdew, *Phys. Rev. B: Condens. Matter Mater. Phys.*, 1986, **33**, 8822–8824.

85 A. D. Becke, *Phys. Rev. A: At., Mol., Opt. Phys.*, 1988, **38**, 3098–3100.

86 E. van Lenthe, E. J. Baerends and J. G. Snijders, *J. Chem. Phys.*, 1993, **99**, 4597–4610.

87 E. van Lenthe, E. J. Baerends and J. G. Snijders, *J. Chem. Phys.*, 1994, **101**, 9783–9792.

88 C. van Wüllen, *J. Chem. Phys.*, 1998, **109**, 392–399.

89 D. A. Pantazis, X. Y. Chen, C. R. Landis and F. Neese, *J. Chem. Theory Comput.*, 2008, **4**, 908–919.

90 A. Klamt and G. Schüürmann, *J. Chem. Soc., Perkin Trans. 2*, 1993, 799–805.

91 S. Grimme, J. Antony, S. Ehrlich and H. Krieg, *J. Chem. Phys.*, 2010, **132**, 154104–154119.

This journal is © the Owner Societies 2014

Phys. Chem. Chem. Phys., 2014, **16**, 11877–11892 | 11891

92 V. N. Staroverov, G. E. Scuseria, J. Tao and J. P. Perdew, *J. Chem. Phys.*, 2003, **119**, 12129–12137.

93 J. Tao, J. P. Perdew, V. N. Staroverov and G. E. Scuseria, *Phys. Rev. Lett.*, 2003, **91**, 146401.

94 L. Noodleman, *J. Chem. Phys.*, 1981, **74**, 5737–5743.

95 K. Yamaguchi, T. Tsunekawa, Y. Toyoda and T. Fueno, *Chem. Phys. Lett.*, 1988, **143**, 371–376.

96 S. Yamanaka, T. Kawakami, H. Nagao and K. Yamaguchi, *Chem. Phys. Lett.*, 1994, **231**, 25–33.

97 A. Bencini and F. Totti, *J. Chem. Theory Comput.*, 2009, **5**, 144–154.

98 M. Orio, D. A. Pantazis and F. Neese, *Photosynth. Res.*, 2009, **102**, 443–453.

99 F. Neese, *J. Comput. Chem.*, 2003, **24**, 1740–1747.

100 F. Neese, F. Wennmohs, A. Hansen and U. Becker, *Chem. Phys.*, 2009, **356**, 98–109.

101 F. Weigend, *Phys. Chem. Chem. Phys.*, 2006, **8**, 1057–1065.

102 M. Orio, D. A. Pantazis, T. Petrenko and F. Neese, *Inorg. Chem.*, 2009, **48**, 7251–7260.

103 P. E. M. Siegbahn, *Acc. Chem. Res.*, 2009, **42**, 1871–1880.

104 S. Luber, I. Rivalta, Y. Umena, K. Kawakami, J.-R. Shen, N. Kamiya, G. W. Brudvig and V. S. Batista, *Biochemistry*, 2011, **50**, 6308–6311.

105 X. Li, E. M. Sproviero, U. Ryde, V. S. Batista and G. Chen, *Int. J. Quantum Chem.*, 2013, **113**, 474–478.

106 M. Retegan, F. Neese and D. A. Pantazis, *J. Chem. Theory Comput.*, 2013, **9**, 3832–3842.

107 Y. Pushkar, J. Yano, P. Glatzel, J. Messinger, A. Lewis, K. Sauer, U. Bergmann and V. K. Yachandra, *J. Biol. Chem.*, 2007, **282**, 7198–7208.

108 Y. L. Pushkar, J. Yano, K. Sauer, A. Boussac and V. K. Yachandra, *Proc. Natl. Acad. Sci. U. S. A.*, 2008, **105**, 1879–1884.

109 H. Dau, A. Grundmeier, P. Loja and M. Haumann, *Philos. Trans. R. Soc. London, Ser. B*, 2008, **363**, 1237–1243.

110 A. Grundmeier and H. Dau, *Biochim. Biophys. Acta, Bioenerg.*, 2012, **1817**, 88–105.

111 F. H. Koua, Y. Umena, K. Kawakami and J.-R. Shen, *Proc. Natl. Acad. Sci. U. S. A.*, 2013, **110**, 3889–3894.

112 M. Sugiura, F. Rappaport, K. Brettel, T. Noguchi, A. W. Rutherford and A. Boussac, *Biochemistry*, 2004, **43**, 13549–13563.

113 H. Dau, J. C. Andrews, T. A. Roelofs, M. J. Latimer, W. Liang, V. K. Yachandra, K. Sauer and M. P. Klein, *Biochemistry*, 1995, **34**, 5274–5287.

114 S. Pudollek, *Doctoral Thesis*, Freie Universität Berlin, 2012.

115 S. Pudollek, F. Lendzian and R. Bittl, *Biochem. Soc. Trans.*, 2008, **36**, 1001–1004.

116 C. Teutloff, S. Kessen, J. Kern, A. Zouni and R. Bittl, *FEBS Lett.*, 2006, **580**, 3605–3609.

117 H. Matsuoka, K. Furukawa, T. Kato, H. Mino, J.-R. Shen and A. Kawamori, *J. Phys. Chem. B*, 2006, **110**, 13242–13247.

118 D. Koulougliotis, R. H. Schweitzer and G. W. Brudvig, *Biochemistry*, 1997, **36**, 9735–9746.

119 G. A. Lorigan and R. D. Britt, *Photosynth. Res.*, 2000, **66**, 189–198.

120 K. A. Campbell, D. A. Force, P. J. Nixon, F. Dole, B. A. Diner and R. D. Britt, *J. Am. Chem. Soc.*, 2000, **122**, 3754–3761.

121 M. Zheng, S. V. Khangulov, G. C. Dismukes and V. V. Barynin, *Inorg. Chem.*, 1994, **33**, 382–387.

122 G. J. Yeagle, M. L. Gilchrist, L. M. Walker, R. J. Debus and R. D. Britt, *Philos. Trans. R. Soc. London, Ser. B*, 2008, **363**, 1157–1166.

123 T. A. Stich, G. J. Yeagle, R. J. Service, R. J. Debus and R. D. Britt, *Biochemistry*, 2011, **50**, 7390–7404.

124 R. J. Debus, K. A. Campbell, W. Gregor, Z. L. Li, R. L. Burnap and R. D. Britt, *Biochemistry*, 2001, **40**, 3690–3699.

125 G. J. Yeagle, M. L. Gilchrist, R. M. McCarrick and R. D. Britt, *Inorg. Chem.*, 2008, **47**, 1803–1814.

126 M. Zheng and G. C. Dismukes, *Inorg. Chem.*, 1996, **35**, 3307–3319.

127 A. Guskov, J. Kern, A. Gabdulkhakov, M. Broser, A. Zouni and W. Saenger, *Nat. Struct. Mol. Biol.*, 2009, **16**, 334–342.

128 X. L. Tan, Y. Gultneh, J. E. Sarneski and C. P. Scholes, *J. Am. Chem. Soc.*, 1991, **113**, 7853–7858.

129 X. S. Tang, M. Sivaraja and G. C. Dismukes, *J. Am. Chem. Soc.*, 1993, **115**, 2382–2389.

130 S. Khangulov, M. Sivaraja, V. V. Barynin and G. C. Dismukes, *Biochemistry*, 1993, **32**, 4912–4924.

131 K.-O. Schäfer, R. Bittl, W. Zweygart, F. Lendzian, G. Haselhorst, T. Weyhermüller, K. Wieghardt and W. Lubitz, *J. Am. Chem. Soc.*, 1998, **120**, 13104–13120.

132 S. Sinnecker, F. Neese, L. Noodleman and W. Lubitz, *J. Am. Chem. Soc.*, 2004, **126**, 2613–2622.

133 S. Sinnecker, F. Neese and W. Lubitz, *J. Biol. Inorg. Chem.*, 2005, **10**, 231–238.

134 T. A. Stich, J. W. Whittaker and R. D. Britt, *J. Phys. Chem. B*, 2010, **114**, 14178–14188.

135 D. T. Edmonds, *Phys. Rep.*, 1977, **29**, 234–290.

136 W. Hillier and T. Wydrzynski, *Phys. Chem. Chem. Phys.*, 2004, **6**, 4882–4889.

11892 | *Phys. Chem. Chem. Phys.*, 2014, **16**, 11877–11892

This journal is © the Owner Societies 2014